A Novel Channel Inconsistency Calibration Algorithm for Azimuth Multichannel SAR Based on Fourth-Order Cumulant

Zhen Liang, Xikai Fu, and Xiaolei Lv, *Member, IEEE*

***Abstract*—In a high-resolution and wide-swath synthetic aperture radar (SAR) platform, the along-track position error reduces the accuracy of the phase error estimation, which will lead to the failure of aliased signal reconstruction. However, classical subspace-based methods require at least one redundant subaperture to construct signal or noise subspace. To overcome this condition, a robust channel error estimation method is presented, which introduces the higher order cumulants to separate these two subspaces by increasing the spatial degree of freedom. First, the M physically existing subapertures are expanded into $2M-1$ virtual channels to construct the noise subspace more accurately. Then, according to the expanded array configuration, the channel error model and the actual steering vector are modified. Finally, based on the orthogonality of signal and noise subspaces, two sets of constrained minimization formulations are constructed. Due to the coupling between these errors, the phase and along-track position errors can be obtained, respectively, by exploiting the idea of alternate iterations. Besides, compared with classical subspace-based methods, the proposed algorithm can avoid the subspace swap phenomenon under condition of low signal-to-noise ratios because the fourth-order cumulant can efficiently suppress additive Gaussian white noise. Finally, the well-focused SAR images, acquired by the four-channel airborne, GF3-01, and GF3-02 SAR systems, demonstrate the feasibility of the proposed error estimation method.**

***Index Terms*—Channel error estimation, channel expansion, fourth-order cumulant (FOC), multichannel synthetic aperture radar (SAR).**

I. Introduction

RECENT years have witnessed an explosion of advances in synthetic aperture radar (SAR) platforms due to its advantages of being independent of time and climate, which has become one of the most important means of retrieving geomorphic information on the Earth's surface [1], [2], [3], [4], [5], [6], [7], [8]. An image with sufficiently high spatial resolution, providing detailed surface scattering characteristics, plays a significant role in target recognition and interpretation. For spaceborne SAR systems, the wide swath is dedicated to completing the global observation in a relatively short time to facilitate the detection of large scenes, such as natural disasters and crop growth. Unfortunately, for the traditional single-channel SAR platforms, it is almost impossible to satisfy both spatial resolution and swath width, which determine the final image quality, under the constraint of minimum antenna area [2]. On the one hand, the spatial resolution can be improved only by reducing the azimuth aperture, and a small antenna size is associated with a high pulse repetition frequency (PRF) to avoid aliasing of the Doppler spectrum [1], [2], [3]. On the other hand, a wide-ranging coverage area consumes a sufficient pulse repetition interval to suppress ambiguity. In response to this dilemma, numerous theoretical studies have advocated that the entire antenna is split into multiple receivers in the along-track direction, which simultaneously receive the wider beam generated by the transmitter, as shown in Fig. 1 [1], [2], [3], [4], [5], [6], [7], [8]. So far, several in-orbit spaceborne dual-channel SAR systems, such as TerraSAR-X, AlOS-2, GF-3 (01, 02),

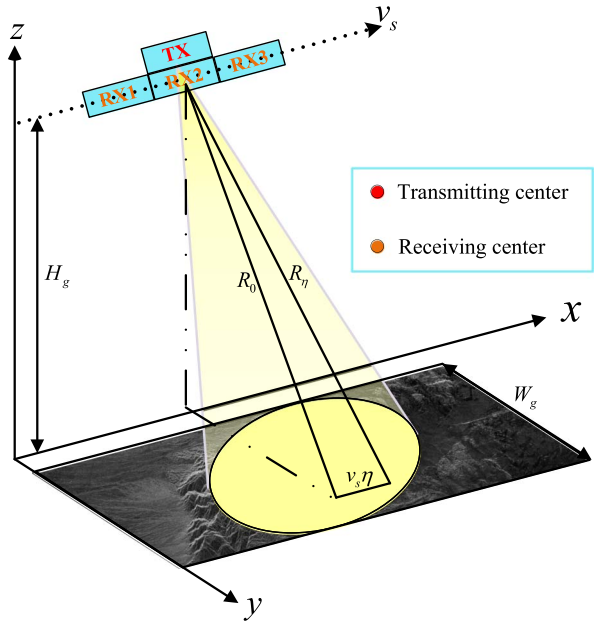

Fig. 1. Imaging geometry of a three-channel SAR platform in azimuth.

Manuscript received 6 April 2023; revised 22 May 2023; accepted 8 June 2023. Date of publication 13 June 2023; date of current version 28 June 2023. This work was supported by the LuTan-1 L-Band Spaceborne Bistatic SAR Data Processing Program under Grant E0H2080702. *(Corresponding author: Xiaolei Lv.)*

Zhen Liang and Xiaolei Lv are with the Key Laboratory of Technology in Geo-Spatial Information Processing and Application System, Aerospace Information Research Institute, Chinese Academy of Sciences, Beijing 100094, China, and also with the School of Electronic, Electrical, and Communication Engineering, University of Chinese Academy of Sciences, Beijing 100049, China (e-mail: liangzhen18@mails.ucas.ac.cn; lvxl@aircas.ac.cn).

Xikai Fu is with the Key Laboratory of Technology in Geo-Spatial Information Processing and Application System, Aerospace Information Research Institute, Chinese Academy of Sciences, Beijing 100094, China (e-mail: xkfu@mail.ie.ac.cn).

Digital Object Identifier 10.1109/JSTARS.2023.3285083

and LuTan-1 (LT-1) [9], have also demonstrated the feasibility of this configuration, which will guide the design of satellite platforms with more subapertures in the future. Ultimately, a wide-coverage SAR image with high spatial resolution is obtained, after Doppler ambiguity caused by undersampling or nonuniform sampling is processed by classical reconstruction algorithms, such as the reconstruction filter [1], [2] and digital beamforming method [3], [4], [5].

Unfortunately, because of nonideal external conditions, such as inconsistent pattern, complex electromagnetic environment, and deformation of the antenna array, systematic errors are inevitably introduced into the satellite payload during the operation of the multichannel SAR platform [3], [6]. In general, systematic errors are usually composed of gain, phase, sampling delay, and position inconsistencies between the receiver phase centers (RPCs) [3], which will induce the steering matrix to deviate from the multichannel signal model and lead to the failure of the reconstruction algorithm. Thus, it can be seen that the accurate compensation for systematic errors between subapertures is crucial for effective reconstruction of nonuniform chirp signals. Compared with other systematic errors, magnitude inconsistency can be calibrated relatively simply through channel equalization, owing to the fact that the signal gain of each subaperture is not coupled in the time domain [6]. The systematic error estimation methods applied to most in-orbit platforms are mainly composed of the time-domain cross-correlation methods and the Doppler domain methods based on the second-order statistics [6], [7], [8], [10], [11], [12], [13], [14], [15], [16].

Time-domain estimation methods (TDEMs) proposed by the authors in [6], [7], and [8] make use of the phase information between adjacent subapertures for spatial interference processing. In order to eliminate the randomness caused by the actual scene, which is composed of a large number of targets and white Gaussian noise, the TDEM tends to average the phase difference. However, the TDEM is usually interfered by incoherent signals generated by other radiation sources, which may increase the variance of channel error along range frequency, especially in the *L*-band. Taking noise and incoherent signals into account, the Doppler domain method has been favored by more and more researchers [10], [11], [12], [13], [14], [15], [16]. Because of the undersampling in azimuth, the Doppler domain method considers that the chip signal of each Doppler bin is composed of aliasing signals from periodic known frequency points [10]. Inspired by the modern array processing technology, under ideal channel configuration, Li et al. [11] first proposed an effective method (OSM) of systematic error compensation by using the principle of orthogonality between noise and signal subspaces. Subsequently, based on the consistency criterion between the signal subspace and the space spanned by the actual manifold matrix, Liang et al. [10] proposed a phase error estimation method (SSM) with a closed-form solution. However, the construction of both noise or signal subspace implies that the dimension of subaperture is larger than the aliasing number of the Doppler spectrum. Meanwhile, subspace-based methods require eigendecomposition of the covariance matrix in each Doppler bin to obtain the eigenvectors, which inevitably increases the time complexity of algorithm. To alleviate this computational load, Guo et al. [12] reconstructed a manifold matrix independent of the Doppler frequency by multiplying a known diagonal matrix to the multichannel data, which required only one eigendecomposition of the covariance matrix. However, in the presence of position error between adjacent subapertures, the diagonal matrix is difficult to compute accurately [17], [18]. The error estimation performance of the above subspace-based methods may degrade rapidly at low signal-to-noise ratios (SNRs) [19], [20] because noise and signal subspaces cannot be precisely distinguished. In order to alleviate the phenomenon of subspace swapping, combined with adaptive array processing algorithms, Zhang et al. [13] maximized the power of each aliased signal retrieved by constructing a series of optimization functions, such as the minimum variance distortionless response (MVDR) beamformer and orthogonal projection methods [14]. Unfortunately, the antenna configuration can no longer be treated as a known uniform linear array under the perturbation of position error, which may interfere with the construction of the weight vector.

Taking into account the insufficient redundancy of subaperture, we introduce the higher order cumulants (HOCs) to meet the demands of increasing spatial degrees of freedom (DOF) and suppressing additive Gaussian noise [21], [22], [23]. First, we provide an explanation of the relationship between second- and higher order statistics in SAR signal processing. Taking a three-channel SAR platform as an example, we further illustrate how the HOCs equivalently expand the number of subapertures from a geometrical perspective. By replacing the covariance matrix with the cumulant matrix, the *M*-channel SAR platform is equivalently extended to $2M$-1 virtual subapertures to increase the DOF. Then, according to the extended antenna configuration, the channel error model and the practical steering vector are modified. After that, according to the principle of orthogonality between the noise and signal subspaces, two sets of constrained minimization functions are constructed to estimate the channel error with high accuracy. Because of the coupling between phase and along-track position errors, the practical steering vector is approximated as the following two parts: the ideal steering vector and the error term of position, by applying the Taylor expansion and ignoring the series above the second order. Based on the idea of alternating iterations, stable solutions for phase and along-track position errors can be obtained, respectively, by solving two sets of constrained minimization formulations. After the phase error of multichannel SAR platform is calibrated, according to the estimated along-track position error, the steering vector is updated in time to complete the reconstruction of the aliased signal, and a high spatial resolution SAR image with wide coverage is obtained.

Compared with the TDEM that applies the expectation operation to suppress noise, the proposed method may obtain better estimation performance since the effect of additive Gaussian white noise can be eliminated by the high-order cumulant, which simultaneously avoids the subspace swap phenomenon under a low SNR condition. Furthermore, compared with subspace-based methods in [10], [11], and [12], the noise subspace can be constructed more accurately exploiting the redundant DOF because the physically existing subapertures are virtually extended through fourth-order cumulants (FOCs). Finally, the diagonal loading technique ensures that matrix $\bar{\mathbf{\Omega}}^T(f_\eta)$ has full rank, which will improve the robustness of error estimation.

The rest of this article is organized as follows. Section II introduces the signal model of multichannel SAR platform in azimuth. In Section III, how high-order cumulants virtually expand the number of subapertures and channel error calibration method are presented in detail. In Section IV, simulation experiment and measured data obtained from airborne and spaceborne SAR platforms are processed to evaluate the performance of the proposed method. Finally, Section V concludes this article.

II. Signal Model of Scene

The antenna of a three-channel SAR platform is divided into three subapertures, which simultaneously receive the wide beam transmitted by the middle sensor. It is assumed that the SAR platform moves along the orbit at a velocity v_s, where H_g represents the altitude of subastral point and R_0 represents the nearest range between the satellite and the target, as shown in Fig. 1 [10], [11], [12]. For a side-looking multichannel SAR platform, the SAR data received by each subaperture can be related with the traditional strip-map mode of self-transmitting and self-receiving by compensating for a constant phase associated with the nearest range R_0 [24].

However, under the influence of the complex electromagnetic environment and the deformation of the antenna sensor, the signal reconstruction will be disturbed by the inconsistencies between the subapertures, which usually include gain, phase, and position deviation [3], [6]. The position deviations of RPCs usually consist of the along-track position deviation and the across-track position deviation [3]. Among them, the across-track position error can be converted into a part of the phase error [12], [13]. We assume that the gain, phase, and position errors of each channel do not change during the observation period of the satellite. Then, the signal received by the mth subaperture in the 2-D time domain can be formulated as follows:

$$s_m(\eta,\tau) \approx \rho_m e^{j\xi_m} s_0\left(\eta + \frac{x_m + \Delta x_m}{2v_s}, \tau\right) \tag{1}$$

where η and τ represent the azimuth slow time and the range fast time, respectively. Definitions ρ_m, ξ_m, and Δx_m are the gain, phase, and along-track position deviation of the mth subaperture with respect to the reference subaperture, respectively. Let $s_0(\eta,\tau)$ represents the envelope of the complex signal measured by a SAR platform of self-transmitting and self-receiving. The along-track position of RPC between the mth subaperture and the reference subaperture can be expressed as

$$x_m = \left(m - \frac{M+1}{2}\right) d \quad 1 \le m \le M \tag{2}$$

where M is the number of subapertures in azimuth and d represents the length of each subaperture. For a multichannel SAR platform, subject to the undersampling in azimuth, the aliasing SAR signal measured at the mth subaperture in the range–Doppler domain can be written as [10]

$$S_m(f_\eta,\tau) \approx \rho_m e^{j\xi_m} \sum_{i=-I}^{I} S_0\left(f_\eta + i\cdot f_p, \tau\right) \times e^{+j\pi(f_\eta + i\cdot f_p)\cdot(x_m+\Delta x_m)/v_s} + N_m(f_\eta,\tau) \tag{3}$$

where $S_0(f_\eta,\tau)$ is the spectrum of signal $s_0(\eta,\tau)$ after the azimuth fast Fourier transform. Let f_p denote low PRF and $f_\eta \in [-f_p/2, f_p/2]$ is the baseband Doppler frequency. Without the loss of generality, the Doppler ambiguity number $(2I+1)$ of the multichannel SAR platform is often less than the number of subapertures for some Doppler bins, which is beneficial to eliminate the influence of Doppler ambiguity on imaging. The index of ambiguity i indicates that the unambiguous signal spectrum $S_0(f_\eta + i\cdot f_p, \tau)$ is folded into the Doppler baseband. The additive Gaussian white noise with zero means is defined as $N_m(f_\eta,\tau)$. Considering the M subapertures of the multichannel SAR platform, the signal output in matrix notation can be reformulated as [10]

$$\boldsymbol{S}(f_\eta,\tau) = \boldsymbol{\Gamma}(\boldsymbol{\gamma})\boldsymbol{A}(f_\eta)\boldsymbol{S_0}(f_\eta,\tau) + \boldsymbol{N}(f_\eta,\tau) \tag{4}$$

where $\boldsymbol{A}(f_\eta)$ denotes an $M \times (2I+1)$ full-rank manifold matrix perturbed by along-track position error, and $\boldsymbol{\Gamma}(\boldsymbol{\gamma})$ is a diagonal matrix of gain–phase error

$$\boldsymbol{S}(f_\eta,\tau) = \left[S_1(f_\eta,\tau),\ldots,S_m(f_\eta,\tau),\ldots,S_M(f_\eta,\tau)\right]^T \tag{5}$$

$$\boldsymbol{\Gamma}(\boldsymbol{\gamma}) = \mathrm{diag}\left[\rho_1 e^{j\xi_1},\ldots,\rho_m e^{j\xi_m},\ldots,\rho_M e^{j\xi_M}\right] \tag{6}$$

$$\boldsymbol{A}(f_\eta) = \left[\boldsymbol{\Gamma_{x,-I}a_{-I}},\ldots,\boldsymbol{\Gamma_{x,i}a_i},\ldots,\boldsymbol{\Gamma_{x,I}a_I}\right] \tag{7}$$

$$\boldsymbol{\Gamma_{x,i}} = \mathrm{diag}\left[e^{+j\pi(f_\eta+i\cdot f_p)\cdot\Delta x_1/v_s},\ldots, e^{+j\pi(f_\eta+i\cdot f_p)\cdot\Delta x_M/v_s}\right] \tag{8}$$

$$\boldsymbol{a_i} = \left[e^{+j\pi(f_\eta+i\cdot f_p)\cdot x_1/v_s},\ldots,e^{+j\pi(f_\eta+i\cdot f_p)\cdot x_m/v_s},\ldots,e^{+j\pi(f_\eta+i\cdot f_p)\cdot x_M/v_s}\right]^T \tag{9}$$

$$\boldsymbol{S_0}(f_\eta,\tau) = \left[S_0\left(f_\eta - I\cdot f_p,\tau\right),\ldots,S_0\left(f_\eta - i\cdot f_p,\tau\right),\ldots,S_0\left(f_\eta + I\cdot f_p,\tau\right)\right]^T \tag{10}$$

$$\boldsymbol{N}(f_\eta,\tau) = \left[N_1\left(f_\eta,\tau\right),\ldots,N_M\left(f_\eta,\tau\right)\right]^T \tag{11}$$

where $\boldsymbol{\Gamma_{x,i}}$ depends on the Doppler frequency f_η, which will degrade the precision of the phase error estimation. $(\bullet)^T$ represents the vector transpose operation and diag$(\bullet)$ represents a diagonal matrix whose main diagonal elements consist of a vector.

III. Channel Expansion and Error Estimation Method

The relationship between the FOC and subaperture expansion is first analyzed. Then, taking into account the coupling of phase and along-track position errors, an improved channel error estimation method is further described in this section.

A. HOCs—Properties

In order to explain the relationship between second- and fourth-order statistics in the SAR signal processing, we temporarily ignore the effect of the phase and along-track position errors between different subapertures. In Section III-A, $\rho_m = 1$, $\xi_m = 0$, and $\Delta x_m = 0$ $(1 \le m \le M)$. Then, an FOC is given

as follows [21], [22], [23]:

$$\begin{aligned}\kappa_{k_1,k_2}^{k_3,k_4} &= \mathrm{Cum}\left(S_{k_1}(f_\eta,\tau), S_{k_2}(f_\eta,\tau), S_{k_3}(f_\eta,\tau), S_{k_4}(f_\eta,\tau)\right)\\ &= \underset{\tau}{E}\left\{S_{k_1}S_{k_2}S_{k_3}^*S_{k_4}^*\right\} - \underset{\tau}{E}\left\{S_{k_1}S_{k_3}^*\right\}\underset{\tau}{E}\left\{S_{k_2}S_{k_4}^*\right\}\\ &\quad -\underset{\tau}{E}\left\{S_{k_1}S_{k_4}^*\right\}\underset{\tau}{E}\left\{S_{k_2}S_{k_3}^*\right\}\\ &\quad -\underset{\tau}{E}\left\{S_{k_1}S_{k_2}\right\}\underset{\tau}{E}\left\{S_{k_3}^*S_{k_4}^*\right\}\\ &\quad 1\le k_1,k_2,k_3,k_4\le M \end{aligned} \tag{12}$$

where S_{k_i} denotes $S_{k_i}(f_\eta,\tau)$ for short, which is the k_i elements of the measured echo signal $\boldsymbol{S}(f_\eta,\tau)$, and $(\bullet)^*$ denotes the conjugate operation. The subspace-based methods usually take advantage of the second-order statistic of the received signal, which is expressed as follows [10], [15]:

$$\mu_{k_1,k_2} = \underset{\tau}{E}\left\{S_{k_1}(f_\eta,\tau)S_{k_2}^*(f_\eta,\tau)\right\} \tag{13}$$

$$\hat{\mu}_{k_1,k_2} = \frac{1}{Nr}\sum_{\tau_k=1}^{Nr} S_{k_1}(f_\eta,\tau_k)S_{k_2}^*(f_\eta,\tau_k). \tag{14}$$

Different from the second-order statistic methods under the assumption of white Gaussian noise, the form of the higher order moment can achieve better performance, which is expressed as [21]

$$\begin{aligned}\mu_{k_1,k_2}^{k_3,k_4} = \underset{\tau}{E}\{&S_{k_1}(f_\eta,\tau)S_{k_2}(f_\eta,\tau)S_{k_3}^*(f_\eta,\tau)\\ &S_{k_4}^*(f_\eta,\tau)\}\end{aligned} \tag{15}$$

$$\hat{\mu}_{k_1,k_2}^{k_3,k_4} = \frac{1}{Nr}\sum_{\tau_k=1}^{Nr} S_{k_1}(f_\eta,\tau_k)\,S_{k_2}(f_\eta,\tau_k)\,S_{k_3}^*(f_\eta,\tau_k)\,S_{k_4}^*(f_\eta,\tau_k). \tag{16}$$

If the noise is spatially white, the covariance matrix of the multichannel SAR signal corresponding to the Doppler frequency f_η can be calculated as follows:

$$\begin{aligned}\boldsymbol{R} &= \underset{\tau}{E}\left\{\boldsymbol{S}(f_\eta,\tau)\boldsymbol{S}^H(f_\eta,\tau)\right\}\\ &= \boldsymbol{A}\cdot\underset{\tau}{E}\left\{\boldsymbol{S_0}(f_\eta,\tau)\boldsymbol{S_0}^H(f_\eta,\tau)\right\}\cdot\boldsymbol{A}^H + \sigma_n^2\boldsymbol{I_M}\\ &= \sum_{i=-I}^{I}\sigma_{0,i}^2\boldsymbol{a_i}\boldsymbol{a_i^H} + \sigma_n^2\boldsymbol{I_M}\end{aligned} \tag{17}$$

where $(\bullet)^H$ represents the vector conjugate transpose operation and $\mathrm{E}_\tau\{\bullet\}$ represents the statistical expectation operation in range. $\boldsymbol{I_M}$ is an $M\times M$ identity matrix and σ_n^2 is the noise power.

The subspace-based methods utilize the structure of (17) to decompose into the signal and noise subspaces, and then estimate the channel error based on the orthogonality of these two subspaces. It is impossible to suppress spatially colored noise in the sample covariance matrix unless the noise covariance matrix is known [23]. Fortunately, HOCs are an effective strategy to restrain Gaussian noise. For HOCs, subaperture extension is another advantage in addition to suppressing Gaussian noise, providing more spatial DOF. This means that the number of virtual observation channels obtained by a multichannel SAR platform is larger than the actual number of subapertures.

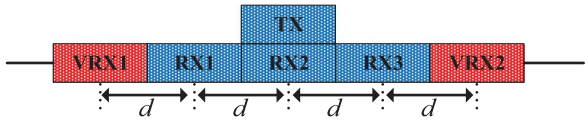

Fig. 2. Virtual aperture extension for three-channel SAR system by FOC.

To provide an explanation of how the FOC expands the number of physically existing subapertures, a configuration of the three-channel SAR platform is presented in Fig. 2. For convenience, the three actual subapertures are represented as $RX1$, $RX2$, and $RX3$, whereas the sensors that measure $VRX1$ and $VRX2$ are defined as virtual subapertures. Cross correlation between the signal $S_1(f_\eta,\tau)$ received by the actual sensor $RX1$ and the signal $S_{v_2}(f_\eta,\tau)$ received by the virtual sensor $VRX2$ (ignoring noise) is defined as virtual cross correlation, assuming $RX2$ is regarded as the reference subaperture

$$\begin{aligned}\mu_{1,v_2} &= \underset{\tau}{E}\left\{S_1(f_\eta,\tau)S_{v_2}^*(f_\eta,\tau)\right\}\\ &= \sum_{i=-1}^{1}\sigma_{0,i}^2\cdot e^{-j\pi(f_\eta+i\cdot PRF)\cdot 3\,d/v_s}\end{aligned} \tag{18}$$

where $\sigma_{0,i}^2$ denotes the power for the ith ambiguous signal $S_0(f_\eta+i\cdot PRF,\tau)$. From (2), the RPC between each subaperture and the reference subaperture is $x_m=-d,0,d$ $(1\le m\le 3)$. Cross correlation can be regarded as the inner product of two random variables in a geometric sense [21]. Hence, $-3\,d$ of (18) provided by the virtual cross correlation represents the positional information between the $RX1$ and $VRX2$. To provide a relationship between the cross correlation and the FOC, consider the following FOC [21], [22]:

$$\begin{aligned}\kappa_{1,1}^{2,3} &= \mathrm{Cum}\left(S_1(f_\eta,\tau)S_1(f_\eta,\tau)S_2^*(f_\eta,\tau)S_3^*(f_\eta,\tau)\right)\\ &= \sum_{i=-1}^{1}\mathrm{Cum}_i\left(S_1S_1S_2^*S_3^*\right)\\ &= \sum_{i=-1}^{1}\gamma_{0,i}\cdot e^{-j\pi(f_\eta+i\cdot PRF)\cdot 3\,d/v_s}\end{aligned} \tag{19}$$

where $\gamma_{0,i}$ denotes the FOC for the ith ambiguous signal $S_0(f_\eta+i\cdot\mathrm{PRF},\tau)$ folded into the Doppler baseband. Then, by comparing (18) and (19), we establish the following connections [21]

(between actual and virtual subapertures):

$$E\left\{S_1S_{v_2}^*\right\} = \sum_{i=-1}^{1}\frac{\sigma_{0,i}^2}{\gamma_{0,i}}\mathrm{Cum}_i\left(S_1S_1S_2^*S_3^*\right). \tag{20}$$

Obviously, it is possible to obtain the positional information of the cross correlation between the actual signal $S_1(f_\eta,\tau)$ and the virtual signal $S_{v_2}(f_\eta,\tau)$ from (20), without using an actual sensor to measure $S_{v_2}(f_\eta,\tau)$. Similarly, we attempt to calculate the cross correlation between other subapertures by using the FOC, which is as follows:

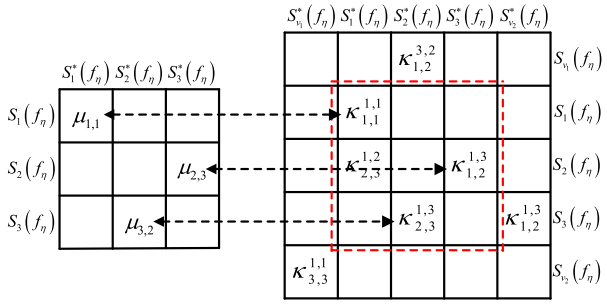

Fig. 3. Relationship between the covariance matrix $\boldsymbol{R}$ and the virtual covariance matrix $\boldsymbol{R_4}$.

(Between actual subapertures)

$$E\left\{S_1 S_2^*\right\} = \sum_{i=-1}^{1} \frac{\sigma_{0,i}^2}{\gamma_{0,i}} \mathrm{Cum}_i\left(S_1 S_1 S_2^* S_1^*\right). \tag{21}$$

(Between virtual subapertures)

$$E\left\{S_{v_1} S_{v_2}^*\right\} = \sum_{i=-1}^{1} \frac{\sigma_{0,i}^2}{\gamma_{0,i}} \mathrm{Cum}_i\left(S_1 S_1 S_3^* S_3^*\right). \tag{22}$$

We replace each cross correlation with the corresponding FOC in covariance matrix of the virtual five channels, which is written as follows:

$$\boldsymbol{R_4} = \sum_{i=-1}^{1} \beta_{0,i}\sigma_{0,i}^2 \boldsymbol{a_i} \boldsymbol{a_i^H} = \sum_{i=-1}^{1} \gamma_{0,i} \boldsymbol{a_i} \boldsymbol{a_i^H}. \tag{23}$$

Comparing (23) with (17), it can be seen that the power of the ith ambiguous signal in the virtual covariance matrix $\boldsymbol{R_4}$ is scaled by $\beta_{0,i}$. It has been demonstrated theoretically and experimentally that the signal subspace of $\boldsymbol{R_4}$ is related to that of $\boldsymbol{R}$ in (17), although the source power of $\boldsymbol{R_4}$ is scaled [23]. Meanwhile, comparing (23) with (17), the additive Gaussian noise is completely suppressed owing to the application of HOCs. From the perspective of subaperture expansion, it is possible to constitute a 5×5 virtual covariance matrix for an azimuth three-channel SAR platform by applying an FOC, as shown in Fig. 3. On the basis of the above analysis, an M-channel SAR platform can be expanded into $2M-1$ virtual subapertures at most, according to the defined FOCs.

B. Channel Error Estimation

According to the extended antenna configuration, the channel error model and the practical steering vector are modified. For an M-channel SAR platform, since $1 \le k_1, k_2, k_3, k_4 \le M$, the $M^2 \times M^2$ cumulative matrix $\boldsymbol{R_4}$ can be constructed as

$$\begin{aligned}\boldsymbol{R_4} = & \sum_{i=-I}^{I} \left(\boldsymbol{\Gamma} \otimes \boldsymbol{\Gamma}^*\right)\left(\boldsymbol{\Gamma_{x,i}} \otimes \boldsymbol{\Gamma_{x,i}}^*\right)\left(\boldsymbol{a_i} \otimes \boldsymbol{a_i^*}\right) \cdot \gamma_{0,i} \\ & \cdot \left(\boldsymbol{a_i} \otimes \boldsymbol{a_i^*}\right)^H \left(\boldsymbol{\Gamma_{x,i}} \otimes \boldsymbol{\Gamma_{x,i}}^*\right)^H \left(\boldsymbol{\Gamma} \otimes \boldsymbol{\Gamma}^*\right)^H \\ = & \boldsymbol{\Gamma}' \boldsymbol{B} \boldsymbol{R_\gamma} \boldsymbol{B}^H (\boldsymbol{\Gamma}')^H \end{aligned} \tag{24}$$

where

$$\boldsymbol{\Gamma}' = \boldsymbol{\Gamma} \otimes \boldsymbol{\Gamma}^* \tag{25}$$

$$\boldsymbol{B}(f_\eta) = \left[\boldsymbol{\Gamma_{x,-I}}' \boldsymbol{b_{-I}}, \ldots, \boldsymbol{\Gamma_{x,i}}' \boldsymbol{b_i}, \ldots, \boldsymbol{\Gamma_{x,I}}' \boldsymbol{b_I}\right] \tag{26}$$

$$\boldsymbol{\Gamma_{x,i}}' = \boldsymbol{\Gamma_{x,i}} \otimes \boldsymbol{\Gamma_{x,i}}^* \tag{27}$$

$$\boldsymbol{b_i} = \boldsymbol{a_i} \otimes \boldsymbol{a_i^*} \tag{28}$$

$$\boldsymbol{R_\gamma} = \mathrm{diag}\left[\gamma_{0,1}, \ldots, \gamma_{0,m}, \ldots, \gamma_{0,M}\right] \tag{29}$$

$$\gamma_{0,i} = \mathrm{Cum}\left(S_{0,i}, S_{0,i}, S_{0,i}, S_{0,i}\right). \tag{30}$$

For simplicity, $S_{0,i}$ denotes the ith ambiguous signal $S_0(f_\eta + i \cdot \mathrm{PRF}, \tau)$, and $\otimes$ denotes the Kronecker product. The row of cumulative matrix $\boldsymbol{R_4}$ is defined by $(k_1-1)M + k_3$, and the column is defined as $(k_4-1)M + k_2$. In other words, the elements of $\boldsymbol{R_4}$ can be indexed as follows [23]:

$$\begin{aligned}&\boldsymbol{R_4}\left((k_1-1)M + k_3, (k_4-1)M + k_2\right) \\ &= \mathrm{Cum}\left(S_{k_1}, S_{k_2}, S_{k_3}, S_{k_4}\right). \end{aligned} \tag{31}$$

Furthermore, the eigendecomposition of cumulant matrix $\boldsymbol{R_4}(f_\eta)$ can be formulated as follows:

$$\boldsymbol{R_4}(f_\eta) = \boldsymbol{U_S} \cdot \boldsymbol{\Sigma_S} \cdot \boldsymbol{U_S^H} + \boldsymbol{U_N} \cdot \boldsymbol{\Sigma_N} \cdot \boldsymbol{U_N^H}. \tag{32}$$

Through eigendecomposition of the cumulative matrix $\boldsymbol{R_4}(f_\eta)$, M^2 eigenvalues are obtained sequentially, among which the larger ones are $(\lambda_1 > \lambda_2 > \cdots > \lambda_{2I+1})$ and the smaller ones are $(\lambda_{2I+2} = \cdots = \lambda_{M^2} \approx 0)$. Here, $\boldsymbol{u_i}$ is the eigenvector spanned by the eigenvalue λ_i. With sufficient channel redundancy, signal subspace $\boldsymbol{U_S} = [\boldsymbol{u_1 u_2} \cdots \boldsymbol{u_{2I+1}}]$ and noise subspace $\boldsymbol{U_N} = [\boldsymbol{u_{2I+2}} \cdots \boldsymbol{u_{M^2}}]$ are constructed separately. As we all know, the signal subspace spanned by the practical steering vector is orthogonal to the noise subspace [11], [13]. Thus

$$\mathrm{span}\left\{\boldsymbol{\Gamma}'\boldsymbol{\Gamma_{x,-I}}'\boldsymbol{b_{-I}}, \ldots, \boldsymbol{\Gamma}'\boldsymbol{\Gamma_{x,i}}'\boldsymbol{b_i}, \ldots, \boldsymbol{\Gamma}'\boldsymbol{\Gamma_{x,I}}'\boldsymbol{b_I}\right\} \perp \boldsymbol{U_N}. \tag{33}$$

Since $\boldsymbol{\Gamma}'$ and $\boldsymbol{\Gamma_{x,i}}'$ are still unknown, we propose to estimate them in the case of finite samples by solving the following cost function:

$$\hat{\boldsymbol{\Gamma}}' = \arg\min \sum_{i=-I}^{I} \boldsymbol{b_i^H} \boldsymbol{\Gamma_{x,i}}'^H \boldsymbol{\Gamma}'^H U_N U_N^H \boldsymbol{\Gamma}' \boldsymbol{\Gamma_{x,i}}' \boldsymbol{b_i}. \tag{34}$$

To facilitate the estimation of gain and phase errors, the diagonal matrix $\boldsymbol{\Gamma}'$ is vectorized into $\boldsymbol{\delta}$ and the ideal steering vector $\boldsymbol{b_i}$ is diagonalized into a matrix $\boldsymbol{Q_i}$, that is

$$\boldsymbol{\delta} = \mathrm{vec}\left(\boldsymbol{\Gamma}'\right) \tag{35}$$

$$\boldsymbol{Q_i'} = \mathrm{diag}\left(\boldsymbol{\Gamma_{x,i}}' \boldsymbol{b_i}\right) \tag{36}$$

$$\boldsymbol{Q_i} = \mathrm{diag}\left(\boldsymbol{b_i}\right). \tag{37}$$

In order to further analyze the influence of position deviation on the solution of phase error, the lth row and lth column element of the extended along-track position error matrix $\boldsymbol{\Gamma_{x,i}}'$ can be expanded by the first-order Taylor as follows:

$$\begin{aligned}&e^{+j\pi \frac{\Delta x_p - \Delta x_q}{v_s}(f_\eta + i \cdot f_p)} \\ &\approx 1 + j\pi \frac{1}{v_s}\left(f_\eta + i \cdot f_p\right)\left(\Delta x_p - \Delta x_q\right) \end{aligned} \tag{38}$$

where $p = \text{ceil}(\frac{l}{M})$, and ceil$(\bullet)$ denotes the smallest integer not less than the specified expression. $q = \text{mod}(l + M - 1, M) + 1$, and mod$(c, e)$ represents the remainder of c divided by e. Substitute (38) into (36), the diagonal matrix $\boldsymbol{Q}_{\boldsymbol{i}}'$ can be reformulated as follows:

$$\boldsymbol{Q}_{\boldsymbol{i}}' = \boldsymbol{Q}_{\boldsymbol{i}} + \boldsymbol{Q}_{\boldsymbol{i}} \cdot \boldsymbol{\Delta} \cdot j\pi \frac{1}{v_s} (f_\eta + i \cdot f_p) \tag{39}$$

where

$$\begin{aligned} \boldsymbol{\Delta} = \; & (\Delta x_1 - \Delta x_1, \Delta x_1 - \Delta x_2, \ldots, \Delta x_1 - \Delta x_M, \\ & \ldots, \Delta x_m - \Delta x_1, \Delta x_m - \Delta x_2, \ldots, \Delta x_m - \Delta x_M, \\ & \ldots, \Delta x_M - \Delta x_1, \Delta x_M - \Delta x_2, \ldots, \Delta x_M - \Delta x_M). \end{aligned} \tag{40}$$

So, the optimization function (34) can be rewritten as follows:

$$\begin{aligned} \hat{\boldsymbol{\delta}} = \; & \arg\min \; \boldsymbol{\delta}^H \sum_{i=-I}^{I} \boldsymbol{Q}_{\boldsymbol{i}}'^H \boldsymbol{U}_{\boldsymbol{N}} \boldsymbol{U}_{\boldsymbol{N}}^H \boldsymbol{Q}_{\boldsymbol{i}}' \, \boldsymbol{\delta} \\ = \; & \arg\min \; \boldsymbol{\delta}^H \sum_{i=-I}^{I} \bar{\boldsymbol{\Omega}}_i \, \boldsymbol{\delta} = \arg\min \; \boldsymbol{\delta}^H \bar{\boldsymbol{\Omega}} \boldsymbol{\delta} \end{aligned} \tag{41}$$

where

$$\bar{\boldsymbol{\Omega}}_i = \boldsymbol{Q}_{\boldsymbol{i}}'^H \boldsymbol{U}_{\boldsymbol{N}} \boldsymbol{U}_{\boldsymbol{N}}^H \boldsymbol{Q}_{\boldsymbol{i}}' \tag{42}$$

$$\boldsymbol{\Omega}_{\boldsymbol{i}} = \boldsymbol{Q}_{\boldsymbol{i}}^H \boldsymbol{U}_{\boldsymbol{N}} \boldsymbol{U}_{\boldsymbol{N}}^H \boldsymbol{Q}_{\boldsymbol{i}}. \tag{43}$$

Since $\boldsymbol{\Omega}_{\boldsymbol{i}}$ is known and $\bar{\boldsymbol{\Omega}}_i$ is unknown, we attempt to establish a relationship between $\bar{\boldsymbol{\Omega}}_i$ and $\boldsymbol{\Omega}_{\boldsymbol{i}}$

$$\begin{aligned} \bar{\boldsymbol{\Omega}}_i = \; & \boldsymbol{\Omega}_{\boldsymbol{i}} + \boldsymbol{\Omega}_{\boldsymbol{i}} \cdot \boldsymbol{\Delta} \cdot j\pi \frac{1}{v_s} (f_\eta + i \cdot f_p) - \boldsymbol{\Delta} \cdot \boldsymbol{\Omega}_{\boldsymbol{i}} \cdot j\pi \frac{1}{v_s} \\ & (f_\eta + i \cdot f_p) + \boldsymbol{\Delta} \boldsymbol{\Omega}_{\boldsymbol{i}} \boldsymbol{\Delta} \pi^2 \frac{1}{v_s^2} (f_\eta + i \cdot f_p)^2. \end{aligned} \tag{44}$$

Take uniform sampling $(f_p = 2v_s/M/d)$ as an example, $|\pi/v_s(f_\eta + i \cdot f_p)| \le (1/2 + i) \cdot 2\pi/M/d$. For a spaceborne SAR satellite system, the entire antenna length (Md) is greater than 2π, so $|\pi/v_s(f_\eta + i \cdot f_p)|$ is close to 1. At the same time, since the along-track position error matrix $\boldsymbol{\Delta}$ is relatively small, in the coarse estimation of phase error, $\bar{\boldsymbol{\Omega}}_i$ is usually treated as approximately equal to $\boldsymbol{\Omega}_{\boldsymbol{i}}$. More precisely, based on the idea of alternating iterations, the entire channel error calibration algorithm is divided into two steps to estimate phase and along-track position errors, respectively. In the first step, initializing the along-track position error $(\boldsymbol{\Delta} = 0)$, the phase error $\boldsymbol{\Gamma}'$ of each Doppler bin is estimated according to the specific ambiguity number. In the next step, the estimated phase error $\boldsymbol{\Gamma}'$ is compensated into the echo signal, and then the along-track position error $\boldsymbol{\Delta}$ is estimated. Finally, $\bar{\boldsymbol{\Omega}}_i$ is updated according to the obtained along-track position error, and the above two steps are iterated multiple times until stable solutions $\boldsymbol{\Gamma}'$ and $\boldsymbol{\Delta}$ are found.

1) Phase Error Calibration: The phase error of multichannel SAR platform can be calculated by solving a set of constrained minimization formulations, that is

$$\begin{aligned} & \min_{\hat{\boldsymbol{\delta}}} \; \hat{\boldsymbol{\delta}}^H \bar{\boldsymbol{\Omega}}(f_\eta) \hat{\boldsymbol{\delta}} \\ & \text{s. t.} \; \boldsymbol{\omega}^H \hat{\boldsymbol{\delta}} = \mathbf{1}_{\boldsymbol{M}} \end{aligned} \tag{45}$$

where $\mathbf{1}_{\boldsymbol{M}}$ is an $(M \times 1)$ matrix of ones. For each Doppler bin f_η, the Lagrange function related to (45) is defined as follows:

$$f_1\left(\hat{\boldsymbol{\delta}}, \boldsymbol{\mu}\right) = \hat{\boldsymbol{\delta}}^H \bar{\boldsymbol{\Omega}}(f_\eta) \hat{\boldsymbol{\delta}} + \boldsymbol{\mu}^H \left(\boldsymbol{\omega}^H \hat{\boldsymbol{\delta}} - \mathbf{1}_{\boldsymbol{M}}\right) \tag{46}$$

where $\boldsymbol{\mu}$ is the Lagrange multiplier. The differential df_1 of a multivariate complex-valued function $f_1(\hat{\boldsymbol{\delta}}, \boldsymbol{\mu}) : \mathbb{C} \to \mathbb{C}$ can be expressed as

$$df_1 = \left(\hat{\boldsymbol{\delta}}^H \bar{\boldsymbol{\Omega}}(f_\eta) + \boldsymbol{\mu}^H \boldsymbol{\omega}^H\right) d\hat{\boldsymbol{\delta}} + \hat{\boldsymbol{\delta}}^T \bar{\boldsymbol{\Omega}}^T(f_\eta) d\hat{\boldsymbol{\delta}}^*. \tag{47}$$

The partial derivative of (46) with respect to $\hat{\boldsymbol{\delta}}$ can be written as

$$\frac{\partial f_1}{\partial \hat{\boldsymbol{\delta}}} = \bar{\boldsymbol{\Omega}}^T(f_\eta) \hat{\boldsymbol{\delta}}^* + \boldsymbol{\omega}^* \boldsymbol{\mu}^*. \tag{48}$$

Setting the first partial derivative equal to zero, we can calculate the Lagrangian multipliers $\boldsymbol{\mu}^* = -(\boldsymbol{\omega}^T(\bar{\boldsymbol{\Omega}}^T(f_\eta))^{-1} \boldsymbol{\omega}^*)^{-1} \mathbf{1}_M$. Then, the extreme point can be written as follows:

$$\hat{\boldsymbol{\delta}}_{f_\eta}^* = \left(\bar{\boldsymbol{\Omega}}^T(f_\eta)\right)^{-1} \boldsymbol{\omega}^* \left(\boldsymbol{\omega}^T \left(\bar{\boldsymbol{\Omega}}^T(f_\eta)\right)^{-1} \boldsymbol{\omega}^*\right)^{-1} \mathbf{1}_M. \tag{49}$$

Finally, the channel errors of the mth subaperture can be indexed as follows:

$$\hat{\rho}_{f_\eta, m} = \text{abs}\left\{\hat{\boldsymbol{\delta}}_{f_\eta}(1 + (m-1)M)\right\}, \; m = 1, 2, \ldots, M \tag{50}$$

$$\hat{\xi}_{f_\eta, m} = \text{angle}\left\{\hat{\boldsymbol{\delta}}_{f_\eta}(1 + (m-1)M)\right\}, \; m = 1, 2, \ldots, M \tag{51}$$

where abs$\{\bullet\}$ and angle$\{\bullet\}$ represent the operations to compute the absolute value and phase of a complex number, respectively. Based on the assumption that the channel error is constant during satellite observation, the gain and phase errors in total Doppler bins are, respectively, averaged as

$$\bar{\rho}_m = \frac{1}{N} \sum_{f_{\eta,i} = f_{\eta,1}}^{f_{\eta,N}} \hat{\rho}_{f_{\eta,i}, m}, \quad m = 1, 2, \ldots, M \tag{52}$$

$$\bar{\xi}_m = \frac{1}{N} \sum_{f_{\eta,i} = f_{\eta,1}}^{f_{\eta,N}} \hat{\xi}_{f_{\eta,i}, m}, \quad m = 1, 2, \ldots, M \tag{53}$$

where N represents the number of samples in azimuth. Subsequently, the raw data of the multichannel SAR platform were compensated as

$$S_m'(f_\eta, \tau) = \frac{1}{\bar{\rho}_m} S_m(f_\eta, \tau) e^{-j\bar{\xi}_m}, \quad m = 1, 2, \ldots, M \tag{54}$$

where $S_m'(f_\eta, \tau)$ represents the aliasing spectrum of the mth subaperture after eliminating the gain and phase deviation. To ensure that the invertible matrix in (49) is not ill-conditioned under the condition of SAR signal model mismatch, we introduce the diagonal loading technique, just as

$$\bar{\boldsymbol{\Omega}}^T(f_\eta) = \bar{\boldsymbol{\Omega}}^T(f_\eta) + \epsilon \boldsymbol{I} \tag{55}$$

where the factor ϵ represents a relatively small real number, such as $\epsilon = 0.1$. Ultimately, after the gain–phase error $\boldsymbol{\Gamma}'$ of each subaperture is roughly calibrated, we estimate the along-track position error $\boldsymbol{\Delta}$.

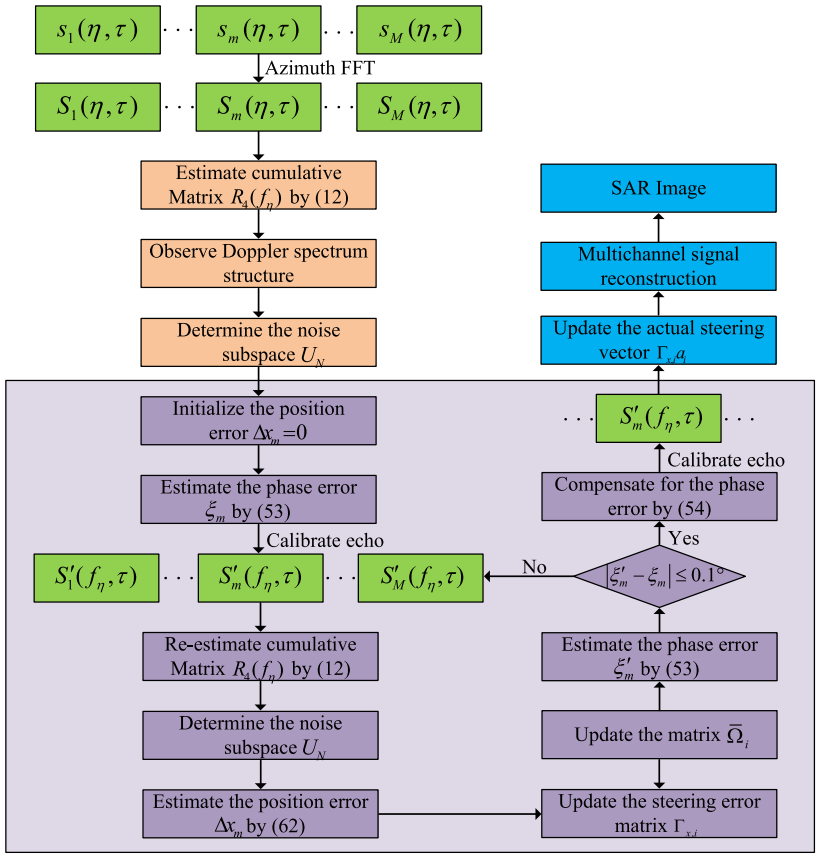

Fig. 4. Flowchart of the improved method.

2) Position Error Calibration: Applying the Taylor expansion and ignoring the series above second order, the extended steering vector $\boldsymbol{\Gamma_{x,i}}'\boldsymbol{b_i}$ can be approximated as the following two parts:

$$\boldsymbol{\Gamma_{x,i}}'\boldsymbol{b_i} = \boldsymbol{b_i} + j\pi\frac{1}{v_s}(f_\eta + i\cdot f_p)\cdot\boldsymbol{Q_i}\cdot\boldsymbol{\Delta}, i = 1,\ \ldots, 2I{+}1. \tag{56}$$

Furthermore, after the gain–phase deviation is roughly eliminated, according to the orthogonality of the signal and noise subspace, i.e., $\boldsymbol{U_N^H}\boldsymbol{\Gamma_{x,i}}'\boldsymbol{b_i} = 0$, we have

$$j\pi\frac{1}{v_s}(f_\eta + i\cdot f_p)\cdot\boldsymbol{U_N^H}\cdot\boldsymbol{Q_i}\cdot\boldsymbol{\Delta} + \boldsymbol{U_N^H}\cdot\boldsymbol{b_i} = 0. \tag{57}$$

The first subaperture is referred to as the reference subaperture without along-track position error, and $\boldsymbol{\alpha} = [1, 0, \ldots, 0, \ldots, 0]^T$ is an $M^2 \times 1$ vector. Then, the estimation of the along-track position error is equivalent to solving the constrained minimization problem

$$\min_{\hat{\boldsymbol{\Delta}}} \|\boldsymbol{O}\hat{\boldsymbol{\Delta}} + \boldsymbol{P}\| \quad \text{s. t. } \boldsymbol{\alpha}^T\hat{\boldsymbol{\Delta}} = 0 \tag{58}$$

where

$$\boldsymbol{O} = \begin{pmatrix} j\pi\frac{1}{v_s}(f_\eta - I\cdot f_p)\cdot\boldsymbol{U_N^H}\cdot\boldsymbol{Q_{-I}} \\ \vdots \\ j\pi\frac{1}{v_s}(f_\eta + i\cdot f_p)\cdot\boldsymbol{U_N^H}\cdot\boldsymbol{Q_i} \\ \vdots \\ j\pi\frac{1}{v_s}(f_\eta + I\cdot f_p)\cdot\boldsymbol{U_N^H}\cdot\boldsymbol{Q_I} \\ 1\ \ 0\ \ 0\ \ \cdots\cdots\cdots\ \ 0 \end{pmatrix} \quad P = \begin{pmatrix} \boldsymbol{U_N^H}\cdot\boldsymbol{b_{-I}} \\ \vdots \\ \boldsymbol{U_N^H}\cdot\boldsymbol{b_i} \\ \vdots \\ \boldsymbol{U_N^H}\cdot\boldsymbol{b_I} \\ 0 \end{pmatrix}. \tag{59}$$

Similar to the solution for phase error, the along-track position error of the constraint minimization problem in (58) can be written as follows:

$$\hat{\boldsymbol{\Delta}}_{f_\eta} = \boldsymbol{O_1}^{-1}\boldsymbol{\alpha}\left(\boldsymbol{\alpha}^T\boldsymbol{O_1}^{-1}\boldsymbol{\alpha}\right)^{-1}\boldsymbol{\alpha}^T\boldsymbol{O_1}^{-1}\boldsymbol{P_1} - \boldsymbol{O_1}^{-1}\boldsymbol{P_1} \tag{60}$$

where $\boldsymbol{O_1}$ and $\boldsymbol{P_1}$ are given by

$$\boldsymbol{O_1} = \boldsymbol{O}^H\boldsymbol{O} + \boldsymbol{O}^T\boldsymbol{O}^*, \qquad \boldsymbol{P_1} = \boldsymbol{O}^H\boldsymbol{P} + \boldsymbol{O}^T\boldsymbol{P}^*. \tag{61}$$

Thus, the along-track position error of the mth subaperture can be indexed by

$$\hat{\Delta}x_{mf_\eta} = \text{real}\{\hat{\boldsymbol{\Delta}}_{f_\eta}(1 + (m-1)M)\},\ m = 1, 2, \ldots, M \tag{62}$$

where real$\{\bullet\}$ represents the real part of a complex number.

Based on the raw echo of the multichannel SAR platform, Fig. 4 shows the detailed steps of the proposed method.

1) Apply fast Fourier transform for raw echo in azimuth.

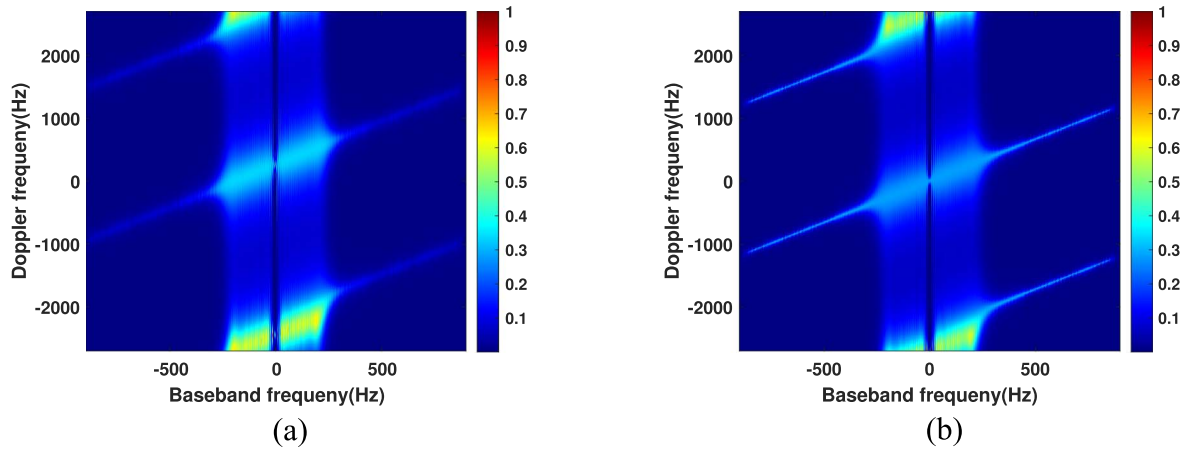

Fig. 5. Ambiguity structure of three-channel SAR platform. (a) Ambiguity structure before phase error calibration. (b) Ambiguity structure after phase error calibration.

2) Calculate cumulative matrix $\hat{\boldsymbol{R}}_{\boldsymbol{4}}(f_\eta)$ by (12).
3) Obtain the ambiguity number at each Doppler frequency f_η.
4) Extract the noise subspace $\boldsymbol{U}_N$ by eigendecomposing $\hat{\boldsymbol{R}}_{\boldsymbol{4}}(f_\eta)$.
5) Initialize the along-track position error $\Delta x_{m,k} = 0$, and $k = 0$.
6) Estimate the phase error $\xi_{m,k}$ by (53), then $k = k + 1$.
7) Compensate it to echo signal by (54).
8) Re-estimate cumulative matrix $\hat{\boldsymbol{R}}_{\boldsymbol{4}}(f_\eta)$ by calibrated echo signal, and update the noise subspace $\boldsymbol{U}_N$.
9) Estimate the position error $\Delta x_{m,k}$ by (62).
10) Update the steering error matrix $\boldsymbol{\Gamma}_{\boldsymbol{x},\boldsymbol{i}}$, and re-estimate the phase error $\xi_{m,k}$.
11) If $|\xi_{m,k} - \xi_{m,k-1}| > 0.1°$, then $k = k + 1$; go to step 7. If $|\xi_{m,k} - \xi_{m,k-1}| \leq 0.1°$, $\xi_m = \xi_{m,k}$ and $\Delta x_m = \Delta x_{m,k}$.
12) Compensate the final phase error to the echo signal by (54), and update the actual steering vector $\boldsymbol{\Gamma}_{\boldsymbol{x},\boldsymbol{i}}\boldsymbol{a}_{\boldsymbol{i}}$.
13) Reconstruct the SAR signal with nonuniform sampling [1], [2], [3], [4], [5].
14) Obtain the wide-coverage SAR image with high spatial resolution [25].

IV. Experimental Results

This section, in the case of insufficient redundancy, verifies the effectiveness of the improved method compared with the conventional subspace-based methods, and then the error performance of simulation experiment with a three-channel SAR platform is analyzed in Section IV-A. In addition, Section IV-B and C validates the accuracy of the proposed method by processing data measured by airborne, GF3-01, and GF3-01 SAR platforms, respectively.

A. Simulation

To quantify the estimated performance of phase and along-track position errors, a three-channel SAR platform in azimuth was adopted. The main parameters of the spaceborne system are listed in Table I, where the PRF and Doppler bandwidth of the system are 1800 and 3598 Hz, respectively. The phase errors of the spaceborne SAR platform are preset as 13.3°, 0.0°, and 47.2°, respectively, as shown in Table II. For subspace-based methods, the Doppler structure of scene is visualized in order to accurately establish the noise or signal subspace. As shown in Figs. 5 and 6(a), the OSM accurately estimated the phase error of these Doppler bins whose ambiguity number is 2, while for Doppler bins with ambiguity number of 3, the estimated result is clearly ill-conditioned. Because the Doppler bins in the middle of Fig. 5 lack sufficient spatial redundancy to completely distinguish signal and noise subspaces. Based on the explanation in Section III-A, the FOC has the properties of subaperture extension and suppression of additive Gaussian noise. In this way, the three-channel SAR system is virtually expanded into five subapertures to increase the DOF and more accurately construct the

TABLE I
Main Parameters of the Simulated SAR System

Parameter	Symbol	Value
Wavelength	λ	0.055517 m
PRF	f_p	1800 Hz
Sampling rate	f_s	133.33 MHz
Signal bandwidth	B_r	100 MHz
Pulse duration	T_r	54.99 μs
Platform velocity	v_s	7614 m/s
Look-angle	θ	35.41°
Channel number	M	3
Adjacent channel interval	d	3.75 m

TABLE II
Phase and Along-Track Errors of the Simulated SAR System

Channel	1	2	3
Phase error	13.3°	0°	47.2°
Position error	0.35 m	0.0 m	-0.18 m

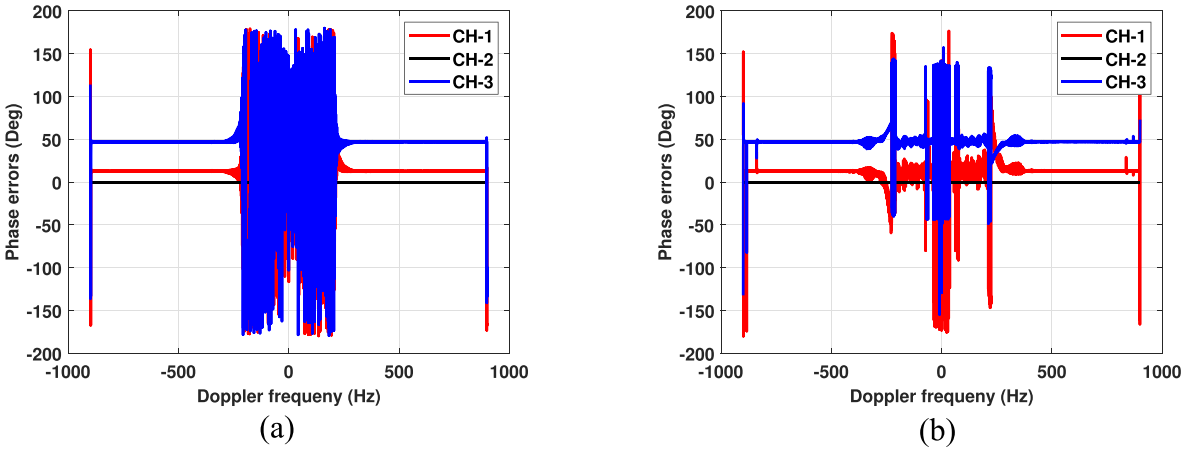

Fig. 6. Simulation results. (a) Phase error estimated by the subspace-based method. (b) Phase error estimated by the proposed method.

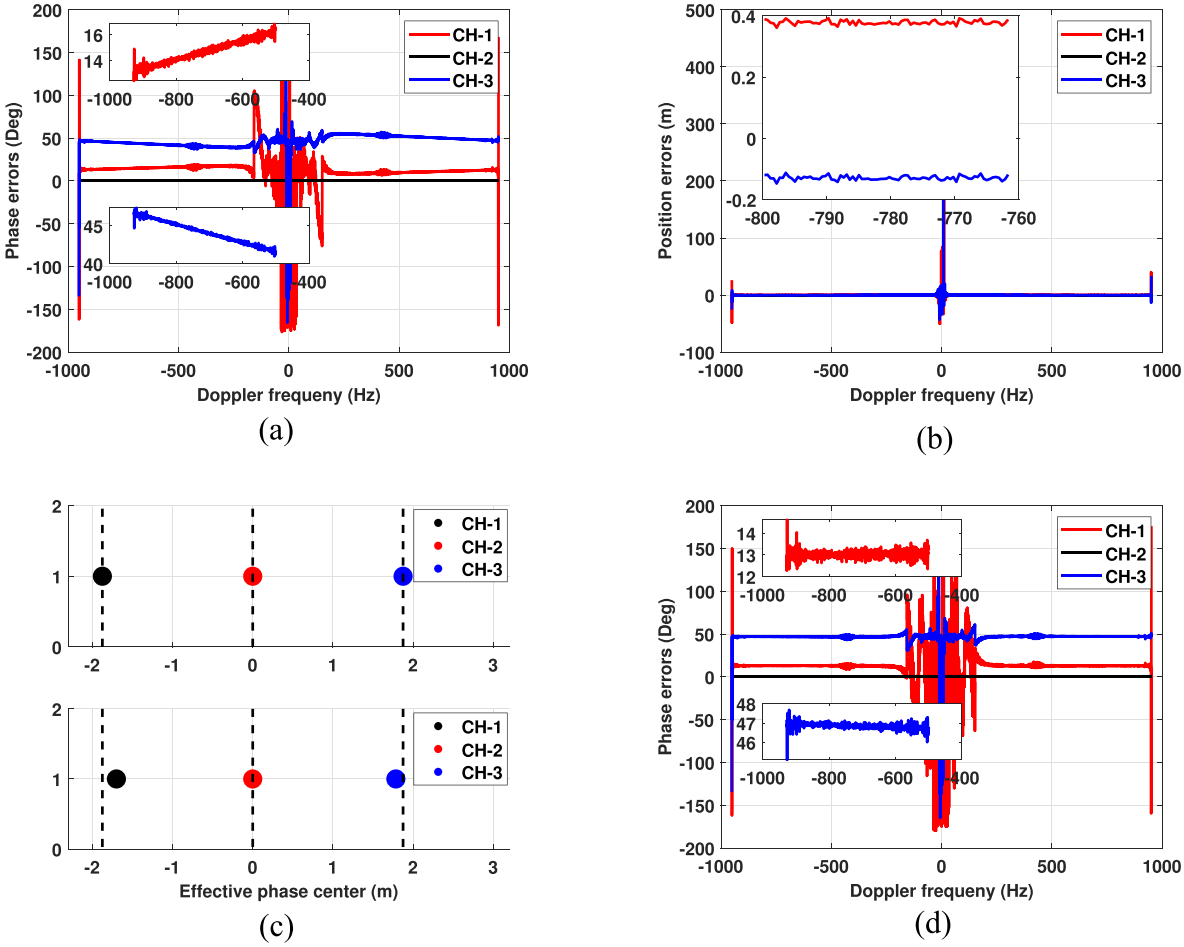

Fig. 7. Simulation results and partial enlargements. (a) Estimated result of the phase error in the first iteration. (b) Estimated result of the along-track position error in the second iteration. (c) Spatial distribution of samples in the three-channel SAR system. (d) Estimated result of the phase error in the second iteration.

noise subspace. It is evident in Fig. 6(b) that the estimated results of phase error for these Doppler bins in the middle have been greatly improved.

Furthermore, on the basis of the above phase error analysis, along-track position deviations are simultaneously preset as 0.35 m, 0.0 m, and −0.18 m. According to the orthogonal criterion between noise and signal subspace, the coarse result of phase error is presented in Fig. 7(a), where it can be seen that the phase error is no longer the artificially preset constants. The linearity of the estimated results is due to the neglect of the residual

TABLE III
ESTIMATION RESULTS OF CLASSICAL METHODS AND PROPOSED METHOD

Channel number	Real phase error	SNR	TDEM	OSM	SSM	MVDR	Proposed method
Channel 1	13.3°	10 dB	15.2673°	15.0737°	14.9921°	14.9507°	12.7784°
		20 dB	14.6723°	14.6266°	14.5879°	14.6469°	13.3276°
		30 dB	14.5492°	14.4731°	14.4342°	14.5431°	13.3402°
Channel 2	0°	10 dB	0.0°	0.0°	0.0°	0.0°	0.0°
		20 dB	0.0°	0.0°	0.0°	0.0°	0.0°
		30 dB	0.0°	0.0°	0.0°	0.0°	0.0°
Channel 3	47.2°	10 dB	45.9173°	46.1648°	46.1693°	46.1952°	46.8247°
		20 dB	46.2729°	46.4794°	46.5362°	46.3457°	47.1663°
		30 dB	46.3637°	46.4976°	46.5769°	46.3564°	47.1847°

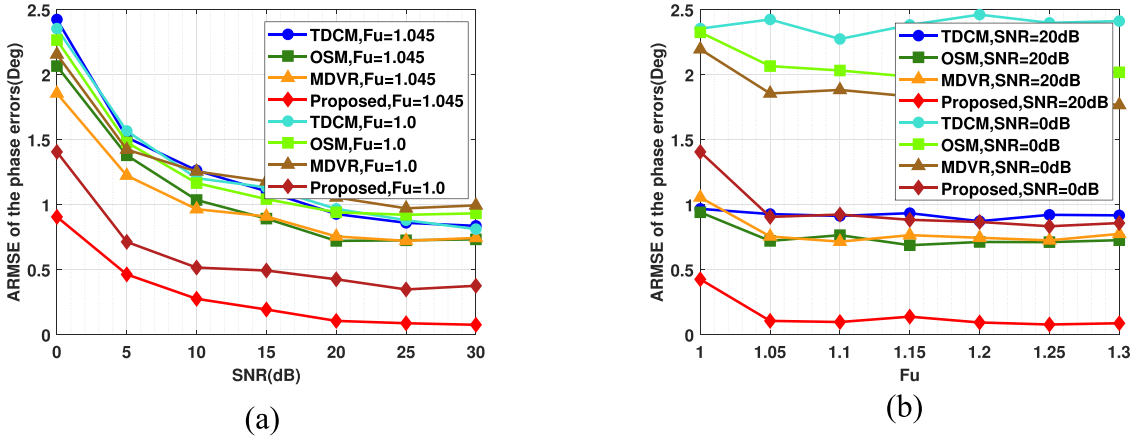

Fig. 8. ARMSE of the phase errors versus SNR and F_u. (a) Versus SNR. (b) Versus F_u.

factor $\boldsymbol{\Delta} \cdot \pi / v_s(f_\eta + i \cdot f_p)$ in the process of $\bar{\boldsymbol{\Omega}}_i \approx \boldsymbol{\Omega}_i$, which is completely inconsistent with our assumption of the along-track position error. According to the flowchart of the proposed algorithm, the along-track position error can be estimated as 0.357 m, 0.0 m, and -0.182 m after two iterations, as shown in Fig. 7(b). After updating the steering vector $\boldsymbol{\Gamma}_{\boldsymbol{x},\boldsymbol{i}}\boldsymbol{a}_{\boldsymbol{i}}$, the recalculated result of the phase error is presented in Fig. 7(d), where it can be seen that the phase error is completely stabilized at the preset value. For different SNRs, the results of phase error calculated by TDEM in [6], OSM in [11], SSM in [10], MVDR in [13], and the proposed method between subapertures are listed in Table III. Obviously, the phase error calculated by the proposed method is closer to the preset value than that calculated by the subspace-based methods. Because the signal subspace spanned by the steering vector $\boldsymbol{\Gamma}_{\boldsymbol{x},\boldsymbol{i}}{}'\boldsymbol{b}_{\boldsymbol{i}}$ disturbed by the along-track position error can be accurately established by multiple iterations. Then, the FOC can suppress the additive Gaussian noise well, which avoids the subspace exchange phenomenon under low SNR conditions.

To demonstrate the robustness of the proposed algorithm, 100 Monte Carlo experiments are performed for different SNRs ranging from 10 to 30 dB. Then, the phase and along-track position errors of the three-channel SAR platform are preset randomly, which are distributed in $[-\pi/3, \pi/3]$ and $[-0.05\,d, 0.05\,d]$, respectively. The average root-mean-square error (ARMSE) is applied to assess the accuracy of error calculation compared with different methods in the 100 Monte Carlo trials, where F_u represents the spatial distribution of the sample [16], [26]. Obviously, compared with the subspace-based methods, the proposed method can still accurately calculate the phase error of SAR platform under the condition of low SNRs, as shown in Fig. 8(a). It is because the proposed method takes advantage of the eigendecomposition of the cumulative matrix $\boldsymbol{R}_{\boldsymbol{4}}$ in (24) to construct the noise subspace, where $\boldsymbol{R}_{\boldsymbol{4}}$ effectively suppresses the additive Gaussian noise and, thus, avoids the phenomenon of signal leakage. At the same time, when estimating the phase error, the interference of the along-track position error is effectively eliminated. Fig. 8(b) shows that, under highly uniform sampling ($F_u \approx 1$), the proposed method takes advantage of the expansion characteristics of aperture to robustly calculate the preset phase error, compared with the traditional method.

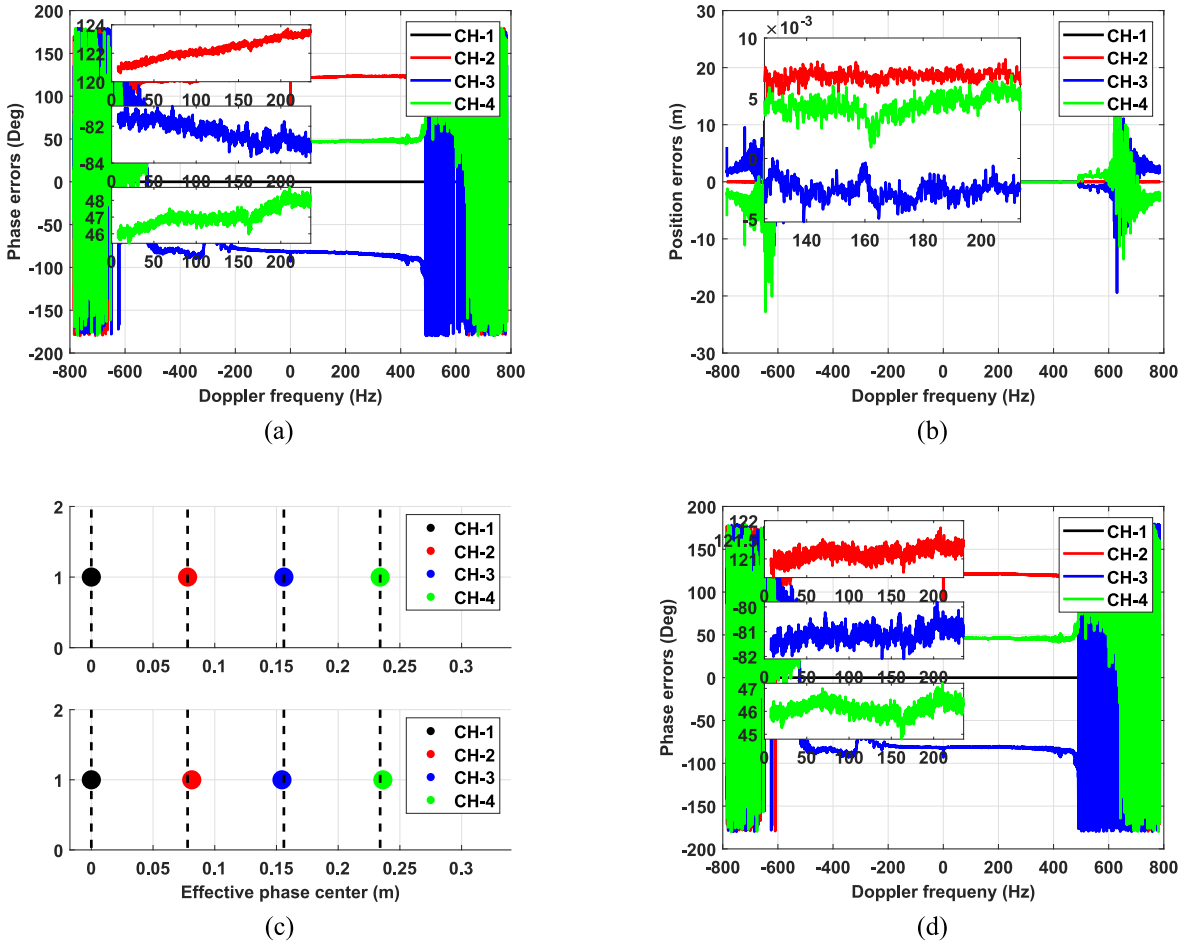

Fig. 9. Estimated results for airborne SAR system and partial enlargements. (a) Estimated result of the phase error in the first iteration. (b) Estimated result of the along-track position error in the second iteration. (c) Spatial distribution of samples in the four-channel SAR system. (d) Estimated result of the phase error in the second iteration.

B. Airborne Data Processing

Airborne data are processed to assess the performance of the proposed algorithm, which was received by the Aerospace Information Research Institute, Chinese Academy of Sciences. The four subapertures of the airborne platform are distributed along the direction of flight, where the first aperture transmits the wide beam, and all apertures simultaneously receive the echo signal. The PRF and Doppler bandwidth of the airborne platform are 1580.67 and 1409.08 Hz, respectively. In order to introduce Doppler ambiguity, the original airborne data are downsampled by a factor of four, and the detailed parameters are presented in Table IV.

Assume that the first subaperture can be regarded as the reference aperture. Under the perturbation of the along-track position deviation, the phase error of the second channel exhibits irregular changes from 117.15° to 123.06°, while the phase error of the third channel, which is affected most dramatically, varies from −77.05° to −89.18°, as shown in Fig. 9(a). These phenomena are not consistent with our model of constant phase error. If the echo signal compensates for the averaged phase error, the residual phase error causes the ambiguous components to appear in azimuth. After the channel error is compensated for the traditional subspace-based method, the well-focused imaging result is shown in Fig. 10(b). It is obvious that the ambiguous component of the strong scatters in Fig. 10(d) still remains, as marked by the red circle.

TABLE IV
MAIN PARAMETERS OF THE AIRBORNE SAR SYSTEM

Parameter	Symbol	Value
Wavelength	λ	0.0556 m
PRF	f_p	395.1694 Hz
Sampling rate	f_s	266.67 MHz
Signal bandwidth	B_r	210 MHz
Pulse duration	T_r	10.40 μs
Platform velocity	v_s	124.05 m/s
Channel number	M	4
Adjacent Channel Interval	d	0.156 m

The interval of phase center between the adjacent receivers is 0.156 m, and the maximum along-track position error after several iterations reaches 0.67 cm, accounting for 4.29%. The geometric distribution of samples in an airborne four-channel SAR platform is further visualized by comparing the ideal and actual channel configurations, as shown in Fig. 9(c), from which it can be observed that the uniform array configuration has been transformed into a nonuniform linear array (NULA).

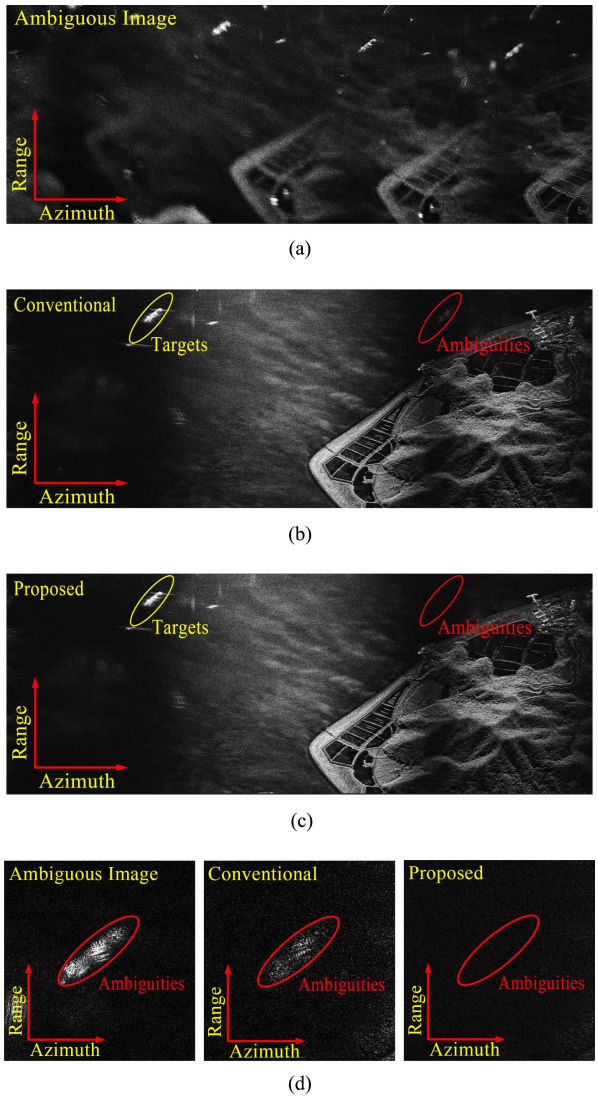

Fig. 10. Imaging results for the airborne four-channel SAR system. (a) Without channel error compensation. (b) Using the classical orthogonal subspace method. (c) Using the proposed method. (d) Partial enlargements of imaging results.

Even if the along-track position error is small (i.e., $\boldsymbol{\Gamma}_{\boldsymbol{x},\boldsymbol{i}} \approx \boldsymbol{I}$), the influence on the accuracy of the phase error estimation cannot be ignored. Taking the along-track position error into account, after two iterations, the phase error of each channel has completely converged, as shown in Fig. 9(d). Fig. 10(c) shows a well-focused SAR image, where Doppler ambiguity is effectively suppressed. Obviously, it can be observed from the local zooming of Fig. 10(d) that the ambiguous area has been basically eliminated.

C. Spaceborne Data Processing

In this section, spaceborne data measured by the GF3 SAR platform, including the GF3-01 satellite launched in August 2016 and the GF3-02 satellite launched in November 2021, are processed to demonstrate the accuracy of error calculation. The main parameters of the dual-channel SAR platform, which operates in strip-map mode, are presented in Table V. Because of its weak backscattering properties, a calm lake is often chosen as a comparison for the scene of Doppler ambiguity, as presented in Fig. 16(b). The scene in the yellow box represents the real target, while the scene in the red box represents the false target caused by Doppler ambiguity. Fig. 11 shows that the Doppler spectrum of the subaperture is basically restored to the same value as that of the reference subaperture after the gain inconsistency is compensated.

TABLE V
MAIN PARAMETERS OF THE GF-3 SAR SYSTEM

Parameter	Symbol	Value
Wavelength	λ	0.055517 m
PRF	f_p	2182.34 Hz
Sampling rate	f_s	133.33 MHz
Signal bandwidth	B_r	80 MHz
Pulse duration	T_r	54.99 μs
Platform velocity	v_s	7480.39 m/s
Look-angle	θ	41.10°
Channel number	M	2
Adjacent channel interval	d	3.75 m

In channel balance, the along-track position errors of GF3-01 and GF3-02 are -0.123 and 0.119 m, respectively, as shown in Figs. 12(b) and 13(b), and the maximum error relative to the interval of RPC is about 3.28%. It can be clearly determined that the spaceborne system is more stable than the airborne system. At the same time, the increase in the number of apertures will further interfere with the accuracy and robustness of phase error estimation. As the index of ambiguity i in (44) increases, the weight of $f_\eta + i \cdot f_p$ will cause $\bar{\boldsymbol{\Omega}}_i$ to deviate from $\boldsymbol{\Omega}_{\boldsymbol{i}}$. According to the flowchart in Fig. 4, after two iterations, the stable solutions of phase error for the GF3-01 and GF3-02 systems are $-156.727°$ and 32.956°, respectively.

Then, we have analyzed in detail the influence of frame dropping of echo signal on channel error estimation. For convenience, we mark the scene in Fig. 13 as scene1 and its adjacent scene as scene2, two of which were collected by the GF3-02 system in a single flight. Taking scene1 as a reference, the phase and along-track position errors of scene2 are $-32.749°$ and -0.832 m, respectively. The interval of RPC between adjacent subapertures is 3.75 m, and the along-track position error accounts for 22.1867%. For adjacent scenes, both orbit and attitude parameters of the satellite are similar, but the estimated results are obviously unreasonable. For scene1, at a certain azimuth sampling time η, the interval of EPC between CH1 and CH2 is $d/2$. However, when the satellite transmits data to the ground receiving station, there will be a small probability of frame dropping. Suppose that at a certain moment η, the echo signal of CH-1 is lost, and we do not know the phenomenon. In this way, we will use the data of CH-2 at this moment η and the data of CH-1 at the next moment $\eta + 1/f_p$ for processing. However, instead of $d/2$, the interval of EPC between these two sample points will be $1/f_p * v_s - d/2$. Therefore, estimating the position deviation with the wrong baseline $d/2$, in the unknown case, will introduce the error of baseline into the along-track position error, which is also the reason why the position error estimated by scene2 increases sharply. Obviously, for the spatial distribution of the samples in Figs. 13(c) and 14(c), the actual

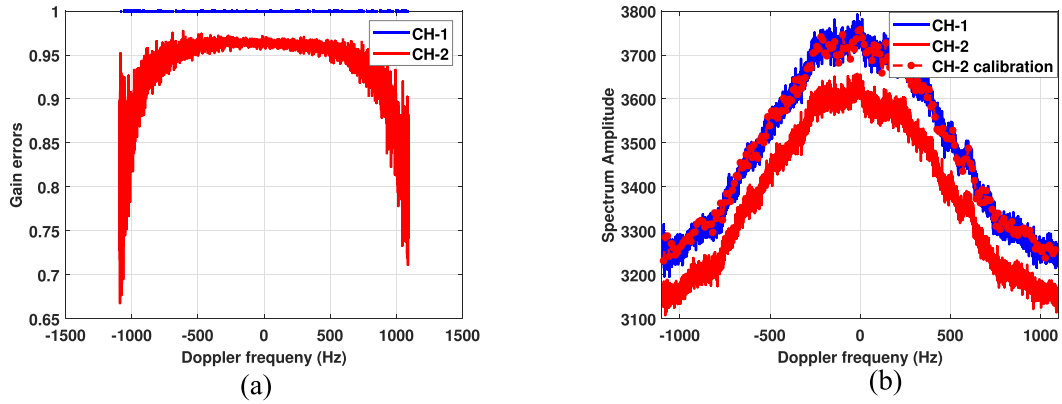

Fig. 11. Gain inconsistency and Doppler spectrum for GF3-02 dual-channel SAR system. (a) Gain error estimated by the proposed method. (b) Doppler spectrum of each subaperture.

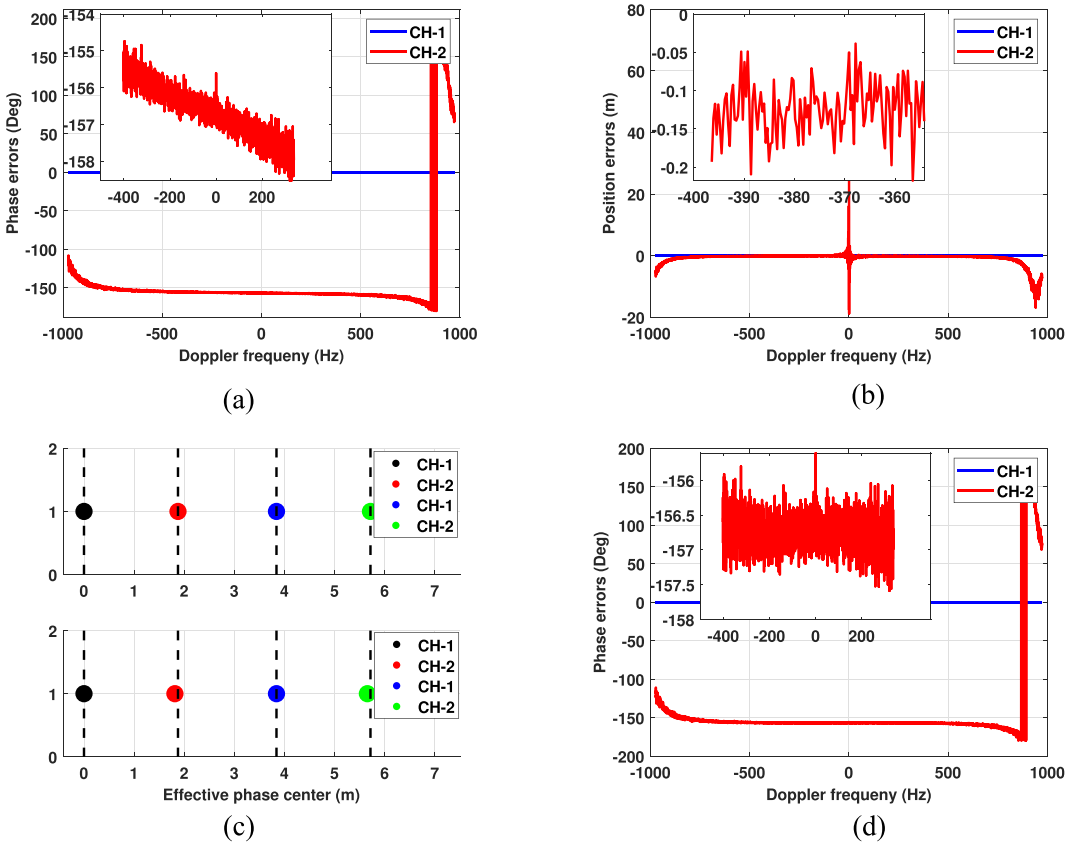

Fig. 12. Estimated results for GF3-01 SAR system and partial enlargements. (a) Estimated result of the phase error in the first iteration. (b) Estimated result of the along-track position error in the second iteration. (c) Spatial distribution of samples in the dual-channel SAR system. (Black and blue represent the EPC of CH-1 samples at time η and $\eta + 1/f_p$, respectively. Red and green similarly represent CH-2.) (d) Estimated result of the phase error in the second iteration.

channel configuration is consistent, except that the data of CH-1 are lost at time η in Fig. 13(c) (black sample). Therefore, especially in the case of frame loss of echo signal, the proposed algorithm is relatively robust.

In view of the phenomenon that the phase errors calculated by some azimuth frequencies are anomalous values, we introduce a diagonal loading technique to ensure that the matrix $\bar{\mathbf{\Omega}}^T(f_\eta)$ in (49) is invertible, as presented in Fig. 15. After the phase error of the multichannel SAR platform is compensated, the actual steering vector $\mathbf{\Gamma}_{x,i}\boldsymbol{a}_i$ is first updated to accommodate the NULA. Finally, after the Doppler ambiguity caused by nonuniform sampling is suppressed, a wide-coverage SAR image with high spatial resolution is obtained by the chirp scaling method [25]. Fig. 16(a) presents the optical image, covering Suya Lake in Henan Province. Obviously, compared with the high spatial resolution image obtained by the conventional OSM, the proposed method completely eliminates the Doppler ambiguity caused by the channel error, as shown in Fig. 16(e).

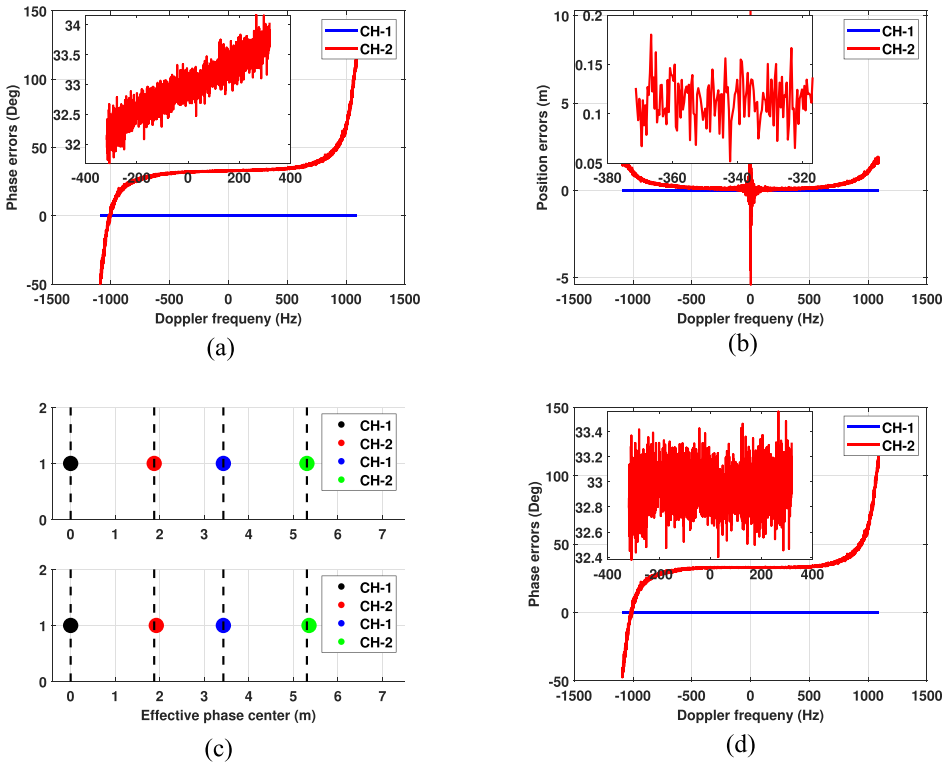

Fig. 13. Estimated results for GF3-02 SAR system scene1 and partial enlargements. (a) Estimated result of the phase error in the first iteration. (b) Estimated result of the along-track position error in the second iteration. (c) Spatial distribution of samples in the dual-channel SAR system. (Black and blue represent the EPC of CH-1 samples at time η and $\eta + 1/f_p$, respectively. Red and green similarly represent CH-2.) (d) Estimated result of the phase error in the second iteration.

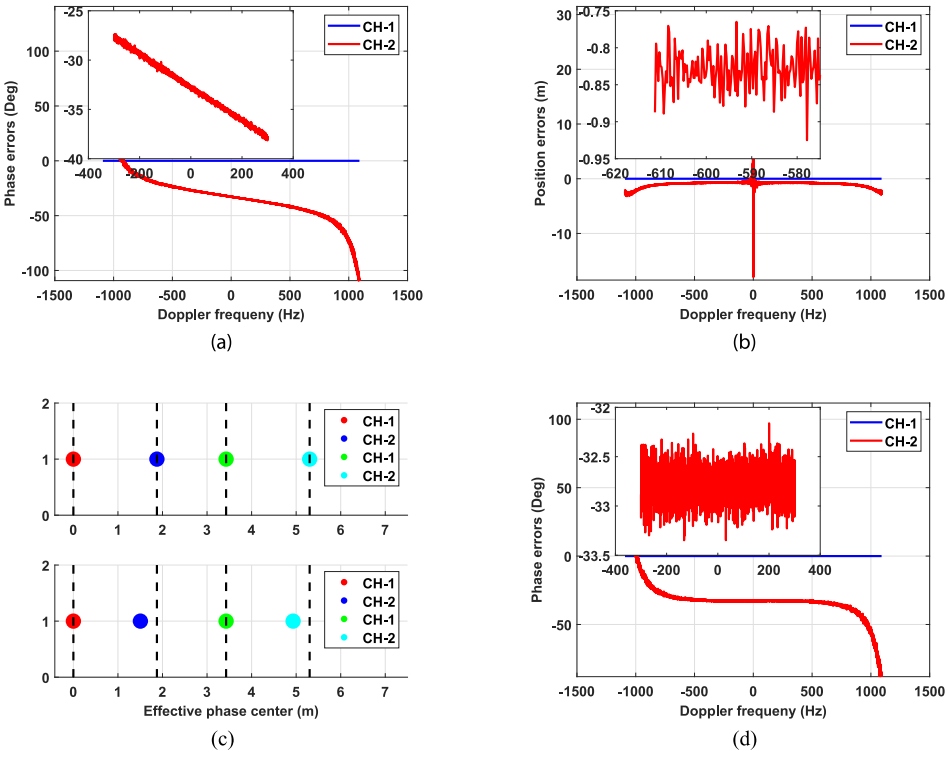

Fig. 14. Estimated results for GF3-02 SAR system scene2 and partial enlargements. (a) Estimated result of the phase error in the first iteration. (b) Estimated result of the along-track position error in the second iteration. (c) Spatial distribution of samples in the dual-channel SAR system. (Red and green represent the EPC of CH-1 samples at time η and $\eta + 1/f_p$, respectively, due to the loss of the true black sample in CH-1. Blue and cyan similarly represent CH-2.) (d) Estimated result of the phase error in the second iteration.

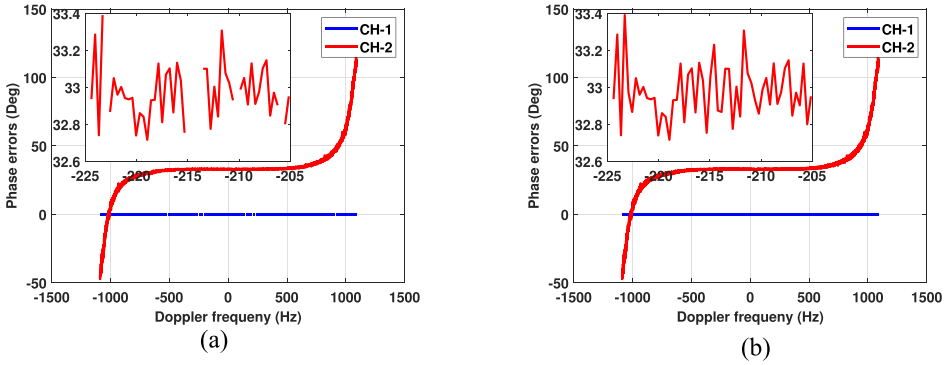

Fig. 15. Estimated results of phase error and partial enlargements. (a) Without the diagonal loading technique. (b) Using the diagonal loading technique.

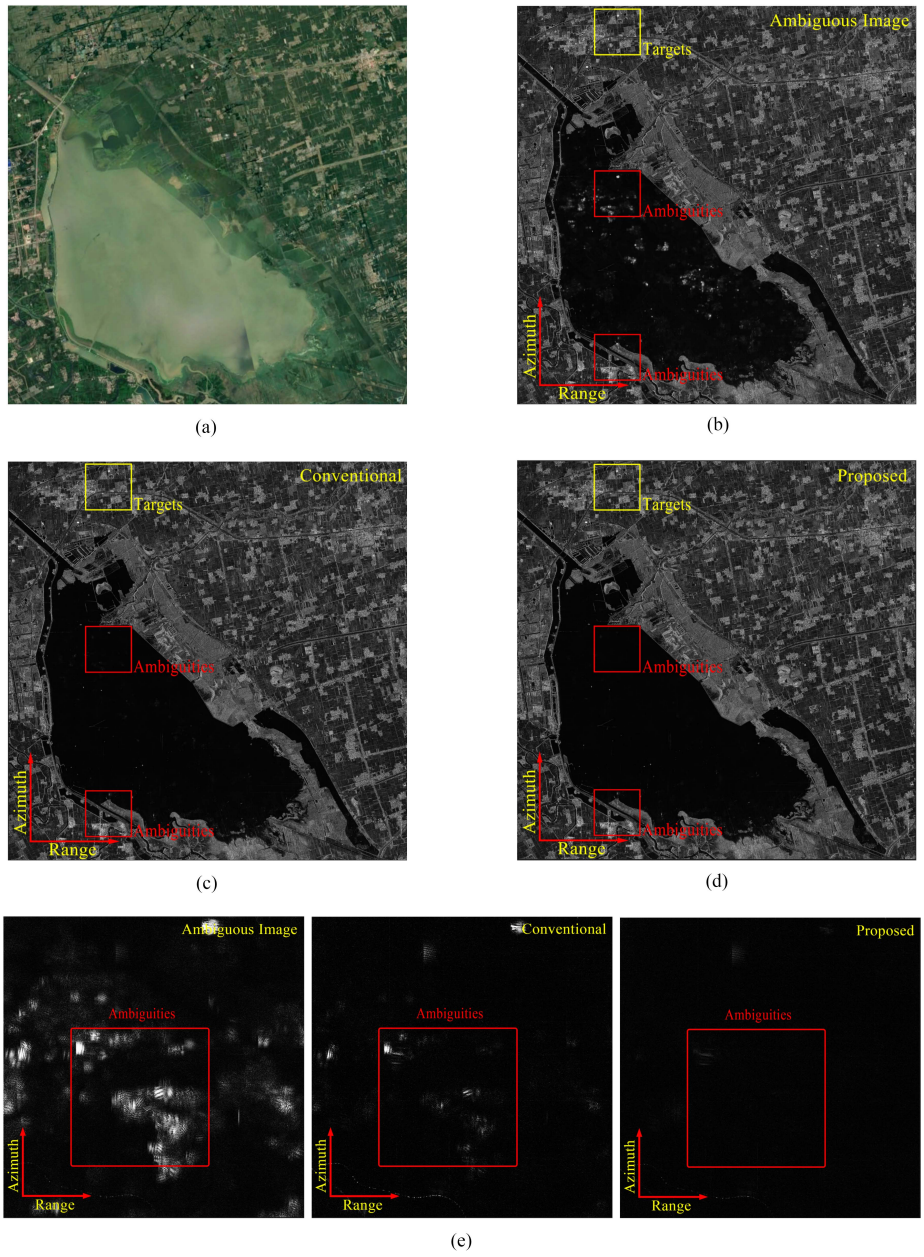

Fig. 16. Imaging results for GF3-02 dual-channel SAR system. (a) Corresponding optical image. (b) Without channel errors calibration. (c) Using the classical orthogonal subspace method. (d) Using the proposed method. (e) Partial enlargements of imaging results.

Therefore, the proposed method is effective to estimate the phase and along-track position errors by virtually expanding the number of channels, which significantly improves the quality of SAR images.

V. Conclusion

In this article, considering the insufficient spatial DOF of the subapertures, an improved channel error estimation method for a multichannel SAR platform has been proposed in the range–Doppler domain. The main contributions of the proposed method are as follows.

1) We provide an interpretation of how HOCs virtually expand the number of subapertures for a multichannel SAR system.
2) The proposed method can accurately establish noise subspace for these Doppler bins with insufficient DOF since the subaperture is virtually expanded by FOC.
3) Considering the disturbance of the along-track position error on the channel geometry, a stable phase error can be accurately estimated by several iterations.
4) The proposed method effectively avoids the subspace exchange phenomenon, especially at low SNRs, because the FOC effectively eliminates additive Gaussian white noise.
5) For the frame dropping of echo data, the proposed method can still work effectively because frame loss is reflected in the along-track position error between adjacent subapertures. Finally, the data analysis of the multichannel airborne/spaceborne SAR platform has verified the feasibility of the proposed error estimation method.

Acknowledgment

The authors would like to thank the Department of Space Microwave Remote Sensing System, Aerospace Information Research Institute, Chinese Academy of Sciences, for providing the four-channel airborne SAR data.

References

[1] G. Krieger, N. Gebert, and A. Moreira, "Unambiguous SAR signal reconstruction from nonuniform displaced phase center sampling," *IEEE Geosci. Remote Sens. Lett.*, vol. 1, no. 4, pp. 260–264, Oct. 2004.
[2] D. Cerutti-Maori, I. Sikaneta, J. Klare, and C. H. Gierull, "MIMO SAR processing for multichannel high-resolution wide-swath radars," *IEEE Trans. Geosci. Remote Sens.*, vol. 52, no. 8, pp. 5034–5055, Aug. 2014.
[3] S.-X. Zhang et al., "Multichannel HRWS SAR imaging based on range-variant channel calibration and multi-Doppler-direction restriction ambiguity suppression," *IEEE Trans. Geosci. Remote Sens.*, vol. 52, no. 7, pp. 4306–4327, Jul. 2014.
[4] B. Liu and Y. He, "Improved DBF algorithm for multichannel high-resolution wide-swath SAR," *IEEE Trans. Geosci. Remote Sens.*, vol. 54, no. 2, pp. 1209–1225, Feb. 2016.
[5] N. Liu, R. Wang, Y. Deng, S. Zhao, and X. Wang, "Modified multichannel reconstruction method of SAR with highly nonuniform spatial sampling," *IEEE J. Sel. Topics Appl. Earth Observ. Remote Sens.*, vol. 10, no. 2, pp. 617–627, Feb. 2017.
[6] J. Feng, C. Gao, Y. Zhang, and R. Wang, "Phase mismatch calibration of the multichannel SAR based on azimuth cross correlation," *IEEE Geosci. Remote Sens. Lett.*, vol. 10, no. 4, pp. 903–907, Jul. 2013.
[7] Y. Liu, Z. Li, Z. Wang, and Z. Bao, "On the baseband Doppler centroid estimation for multichannel HRWS SAR imaging," *IEEE Geosci. Remote Sens. Lett.*, vol. 11, no. 12, pp. 2050–2054, Dec. 2014.
[8] M. Shang, X. Qiu, B. Han, C. Ding, and Y. Hu, "Channel imbalances and along-track baseline estimation for the GF-3 azimuth multichannel mode," *Remote Sens.*, vol. 11, no. 11, 2019, Art. no. 1297.
[9] C. Li et al., "Focusing the L-band spaceborne bistatic SAR mission data using a modified RD algorithm," *IEEE Trans. Geosci. Remote Sens.*, vol. 58, no. 1, pp. 294–306, Jan. 2020.
[10] Z. Liang, X. Fu, and X. Lv, "New channel errors estimation method for multichannel SAR based on virtual calibration source," *Remote Sens.*, vol. 13, no. 18, 2021, Art. no. 3625.
[11] Z. Li, Z. Bao, H. Wang, and G. Liao, "Performance improvement for constellation SAR using signal processing techniques," *IEEE Trans. Aerosp. Electron. Syst.*, vol. 42, no. 2, pp. 436–452, Apr. 2006.
[12] X. Guo, Y. Gao, K. Wang, and X. Liu, "Improved channel error calibration algorithm for azimuth multichannel SAR systems," *IEEE Geosci. Remote Sens. Lett.*, vol. 13, no. 7, pp. 1022–1026, Jul. 2016.
[13] L. Zhang, Y. Gao, and X. Liu, "Robust channel phase error calibration algorithm for multichannel high-resolution and wide-swath SAR imaging," *IEEE Geosci. Remote Sens. Lett.*, vol. 14, no. 5, pp. 649–653, May 2017.
[14] H. Huang et al., "A novel channel errors calibration algorithm for multichannel high-resolution and wide-swath SAR imaging," *IEEE Trans. Geosci. Remote Sens.*, vol. 60, pp. 1–19, Feb. 2022, Art. no. 5201619, doi: 10.1109/TGRS.2021.3053659.
[15] Y. Zhou et al., "A novel approach to Doppler centroid and channel errors estimation in azimuth multi-channel SAR," *IEEE Trans. Geosci. Remote Sens.*, vol. 57, no. 11, pp. 8430–8444, Nov. 2019.
[16] T. Yang, Z. Li, Y. Liu, and Z. Bao, "Channel error estimation methods for multichannel SAR systems in azimuth," *IEEE Geosci. Remote Sens. Lett.*, vol. 10, no. 3, pp. 548–552, May 2013.
[17] P. Huang, X.-G. Xia, X. Liu, X. Jiang, J. Chen, and Y. Liu, "A novel baseline estimation method for multichannel HRSW SAR system," *IEEE Geosci. Remote Sens. Lett.*, vol. 16, no. 12, pp. 1829–1833, Dec. 2019.
[18] M. Shang et al., "The space-time variation of phase imbalance for GF-3 azimuth multichannel mode," *IEEE J. Sel. Topics Appl. Earth Observ. Remote Sens.*, vol. 13, pp. 4774–4788, Aug. 2020, doi: 10.1109/JSTARS.2020.3017048.
[19] J. Yang, X. Qiu, M. Shang, L. Zhong, and C. Ding, "Phase imbalance estimation for azimuth multi-channel ScanSAR system," *IEEE J. Sel. Topics Appl. Earth Observ. Remote Sens.*, vol. 14, pp. 3875–3886, Mar. 2021, doi: 10.1109/JSTARS.2021.3069864.
[20] H. Gao, J. Chen, W. Liu, C. Li, and W. Yang, "Phase inconsistency error compensation for multichannel spaceborne SAR based on the rotation-invariant property," *IEEE Geosci. Remote Sens. Lett.*, vol. 18, no. 2, pp. 301–305, Feb. 2021.
[21] M. C. Dogan and J. M. Mendel, "Applications of cumulants to array processing: I—Aperture extension and array calibration," *IEEE Trans. Signal Process.*, vol. 43, no. 5, pp. 1200–1216, May 1995.
[22] N. Yuen and B. Friedlander, "DOA estimation in multipath: An approach using fourth-order cumulants," *IEEE Trans. Signal Process.*, vol. 45, no. 5, pp. 1253–1263, May 1997.
[23] W.-J. Zeng, X.-L. Li, and X.-D. Zhang, "Direction-of-arrival estimation based on the joint diagonalization structure of multiple fourth-order cumulant matrices," *IEEE Signal Process. Lett.*, vol. 16, no. 3, pp. 164–167, Mar. 2009.
[24] Y. Cai, Y. Deng, H. Zhang, R. Wang, Y. Wu, and S. Cheng, "An image-domain least L 1-norm method for channel error effect analysis and calibration of azimuth multi-channel SAR," *IEEE Trans. Geosci. Remote Sens.*, vol. 60, Feb. 2022, Art. no. 5222914, doi: 10.1109/TGRS.2022.3150797.
[25] A. Moreira, J. Mittermayer, and R. Scheiber, "Extended chirp scaling algorithm for air- and spaceborne SAR data processing in stripmap and ScanSAR imaging modes," *IEEE Trans. Geosci. Remote Sens.*, vol. 34, no. 5, pp. 1123–1136, Sep. 1996.
[26] Y.-Y. Liu, Z.-F. Li, T.-L. Yang, and Z. Bao, "An adaptively weighted least square estimation method of channel mismatches in phase for multichannel SAR systems in azimuth," *IEEE Geosci. Remote Sens. Lett.*, vol. 11, no. 2, pp. 439–443, Feb. 2014.

Zhen Liang received the B.S. degree in optoelectronic information science and engineering from Xidian University, Xi'an, China, in 2018. He is currently working toward the Ph.D. degree in signal and information processing with the Key Laboratory of Technology in GeoSpatial Information Processing and Application System, Aerospace Information Research Institute, Chinese Academy of Sciences, Beijing, China.

He is currently with the University of Chinese Academy of Sciences, Beijing, China. His research interests include the high-resolution wide-swath synthetic aperture radar signal processing.

Xikai Fu received the B.S. degree in electronic and information engineering from Shandong University, Jinan, China, in 2014, and the Ph.D. degree in signal and information processing from the University of Chinese Academy of Sciences, Beijing, China, in 2019.

In 2019, he joined the Aerospace Information Research institute Chinese Academy of Sciences (AIRCAS). His research interests include spaceborne bistatic synthetic aperture radar imaging and interferometry.

Xiaolei Lv (Member, IEEE) received the B.S. degree in computer science and technology and the Ph.D. degree in signal processing from Xidian University, Xi'an, China, in 2004 and 2009, respectively.

From 2009 to 2010, he was with the School of Electrical and Electronic Engineering, Nanyang Technological University, Singapore. From 2011 to 2013, he was with the Department of Civil and Environmental Engineering, Rensselaer Polytechnic Institute, Troy, NY, USA. Since April 2013, he has been with the Institute of Electronics, Chinese Academy of Sciences, Beijing, China. He is also with the University of Chinese Academy of Sciences, Beijing, China. His research interests include sparse signal processing, radar imaging, such as synthetic aperture radar (SAR) and inverse SAR, interferometric SAR, and ground moving-target indication.